New Antenna Calibration Techniques in the Deep Space Network

D. Rochblatt,[1] P. Richter,[2] P. Withington,[3] M. Vazquez,[4] and J. Calvo[4]

This work describes the development of new automated antenna calibration instrumentation for the Deep Space Network (DSN). The purpose of the antenna calibration instrumentation is to provide reliable tools for the assessment, calibration, and improvement of the performance of the large number of antenna systems in the DSN, with special emphasis on Ka-band (32-GHz) performance of the 34-m beam-waveguide (BWG) antennas. The work describes the analysis that was done to characterize the various mechanisms that contribute to noise in the measurements. The results from the analysis led to design and development of a research and development calibration system that utilized the on-the-fly-mapping technique and was deployed at the DSN complex in Goldstone, California. Early results for calibration of the DSN ground antennas and the Cassini onboard radar as a radiometer are presented and agree well with analytical predictions. The system was further used in conjunction with a new fourth-order pointing model to achieve a record blind-pointing performance of the 34-m BWG antennas. The article concludes with a description of the design and implementation of an automated antenna calibration system based on these principles for the DSN: the Antenna Calibration and Measurement Equipment (ACME).

I. Introduction

The NASA–JPL Deep Space Network (DSN) of large, dual-reflector, Earth-based antennas is subject to continuing demands for improved performance, performance evaluation, and reliability as a result of communications, control, and radio science requirements for future missions. The DSN provides the basic communications links with the many spacecraft that form part of the nation's unmanned space exploration program. In order to satisfactorily carry out this mission, each antenna must undergo various calibrations to ensure that it is operating in the most efficient manner possible, and hence delivering maximum information at minimum cost.

[1] Communications Ground Systems Section.

[2] Retired, Communications Architectures and Research Section.

[3] Measurement, Integration, and Test Section.

[4] Madrid Deep Space Communications Complex, Spain.

As part of the strategy of improving the overall performance capability of the DSN, there has been a steady increase in the operating frequency of these antennas over the years, going from frequencies of ~2.3 GHz (S-band), to ~8.4 GHz (X-band), and most recently to ~32 GHz (Ka-band). One can gain a better appreciation of the implications of these frequency increases for antenna calibration by considering the corresponding wavelengths, λ, of the radiation: for S-band, $\lambda \sim 13$ cm; for X-band, $\lambda \sim 3.6$; and for Ka-band, $\lambda \sim 0.9$ cm. The essential performance characteristics of an antenna, such as pointing capability and aperture efficiency, are strongly dependent on the wavelength of the radiation being detected. That is why the large decrease (14:1) in wavelength has resulted in the need for much greater precision of parameters such as reflector surface figure, azimuth track smoothness, and subreflector and beam-waveguide (BWG) mirror alignments.

This article describes the development of antenna calibration instrumentation. The purpose of the antenna calibration instrumentation is to provide reliable tools for the assessment, calibration, and improvement of the performance of the large number of antenna systems in the DSN. Utilizing the principles of noise temperature measurements, the instrumentation measures and derives the antenna gain, systematic pointing corrections, and subreflector focus, as well as the calibration of radio stars[5] used in the antenna gain assessment. The alignments of the antenna main reflector panels and the antenna stability are best measured by coherent holographic techniques.

As a consequence, a new generation of 34-m BWG antennas is being added to the existing complement of 34-m and 70-m Cassegrain-like antennas (shaped reflectors), retrofitted with X-band (8.42-GHz) and Ka-band (32-GHz) transmitting and receiving systems.

As a result of a systematic analysis of the entire measurement procedure, with particular attention to the noise characteristics of the total power radiometer (TPR) [Figs. 1 through 3], plus the tropospherically induced radiometer fluctuations, and the implementation of new techniques for data acquisition and reduction, it has been possible to obtain measurement precision yielding up to an order of magnitude improvement over previous methods in the determination of antenna aperture efficiency and a factor of five or more in the determination of pointing errors and antenna beamwidth. This improvement has been achieved by performing continuous, rapid raster scans of both extended and point radio sources, which is termed on-the-fly (OTF)-mapping.

The advantages of the OTF-mapping technique over the traditional or boresight approach include the following:

(1) It removes a major source of error in determining antenna efficiency by eliminating the need for independently derived source-size correction factors.

(2) In determining the optimum integration time during continuous scan measurements, the actual spectrum of the total power radiometer noise fluctuations is taken into account. This includes radiometer flicker noise and tropospheric turbulence effects.

(3) It provides a direct comparison of the flux density of one radio source with that of another, thus enabling the accurate calibration of many radio sources for future antenna calibrations.

(4) A highly accurate, repeatable, and fully automated system will provide reductions in cost and improve the reliability of antenna performance.

While other calibration techniques have advantages for certain applications, OTF-mapping accurately provides all of the required calibration data in the shortest measurement period, including the beam shape

---

[5] The term "radio star" refers to any natural, compact source of radiation, which, for example, may actually be a remote galaxy of stars, a region of bright microwave emission in our own Milky Way galaxy, or a planet in our solar system.
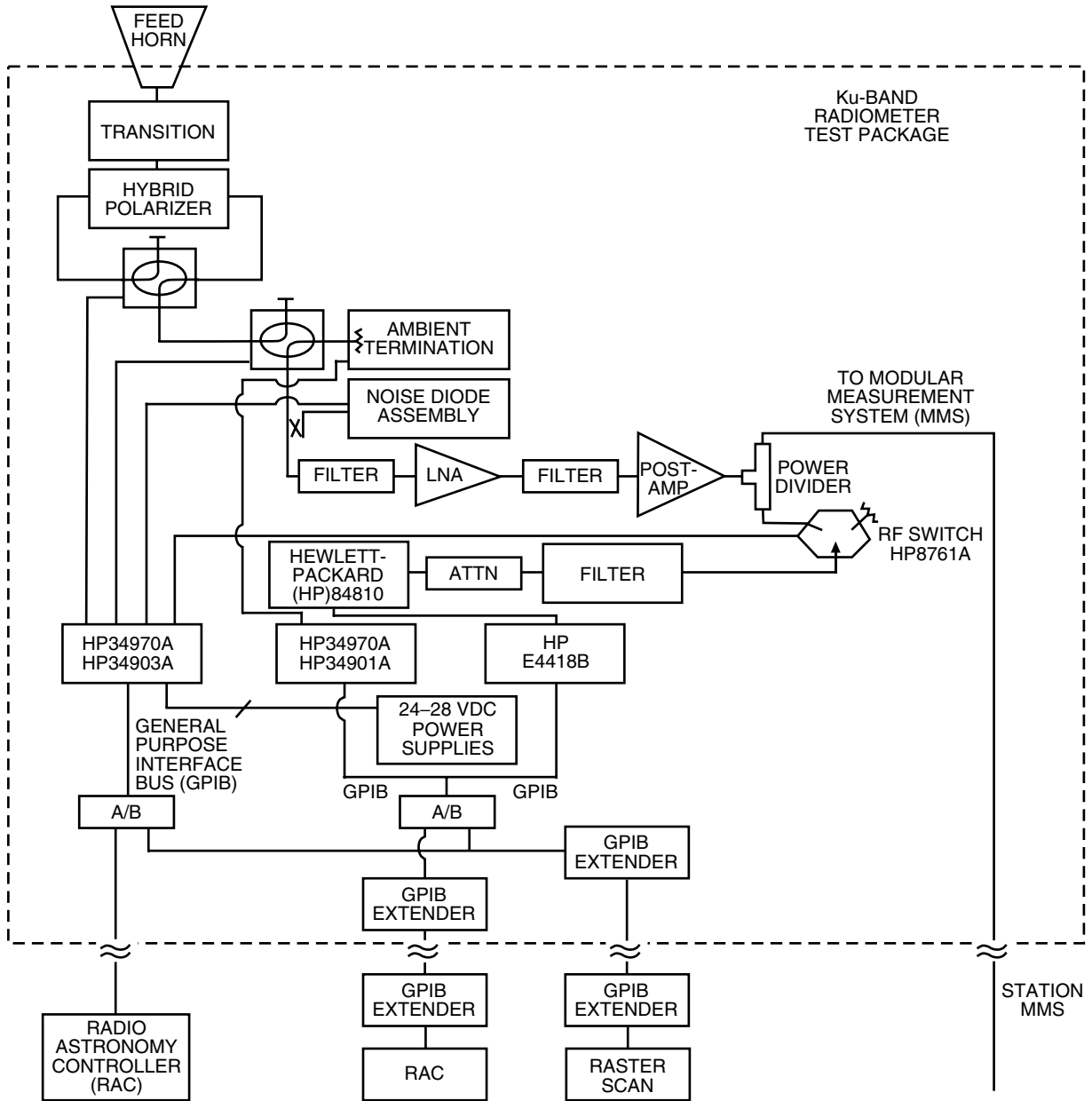
Fig. 1. Block diagram of a TPR designed for operation with the 34-m-diameter BWG antenna at DSS 13 at 13.8 GHz.

and the source flux density. The significance of improvements in antenna calibration, performance, or performance evaluation in the DSN can be put in perspective by recognizing that each decibel of improvement in the quantity gain over noise temperature (G/T) is estimated to be worth about U.S. \$160M/dB in terms of mission support capability [1].

In the following section, we describe the general requirements for the DSN antenna calibration effort. This is followed by a discussion of current methods and their shortcomings, and a final section describes the new approach now being taken in delivering operational Antenna Calibration and Measurement Equipment (ACME) to the DSN.

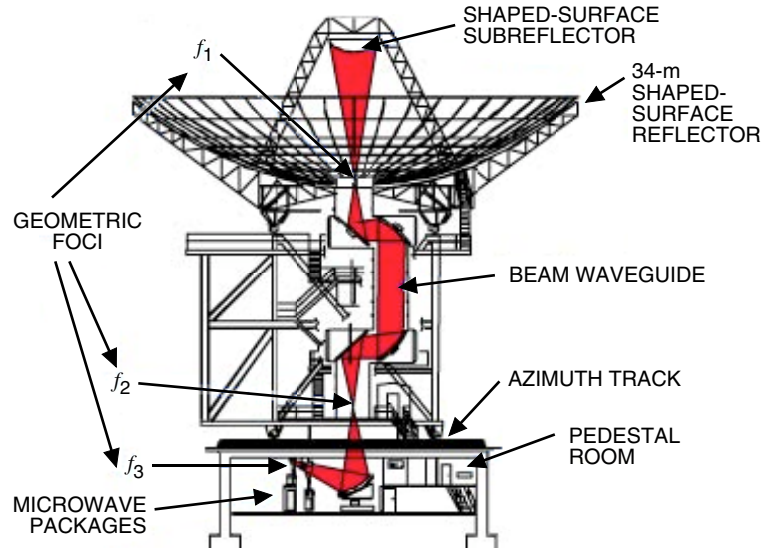**Fig. 2. The 13.8-GHz TPR during testing prior to installation at DSS 13 at f_3.**

Fig. 3. Schematic of a 34-m BWG antenna, indicating placement at the microwave packages' f_3 focus.

II. Calibration System Requirements

The performance of a DSN antenna must be accurately characterized at the time it comes online as a new instrument and when new upgrade capabilities are being implemented. Also, certain characteristics must be checked periodically to maintain performance as well as assess the cause of, and correction for, any observed anomaly during normal tracking of a spacecraft.

Calibration procedures require accurate measurement of the various parameters of interest. In the case of antenna calibration, these fall naturally into two categories, namely, those derivable from the measurement of amplitude and phase of a received coherent microwave signal and those derivable from the measurement of received power from a noncoherent source such as a radio star. The former case involves the interference of received signals from the antenna under test (AUT), and a small reference antenna mounted nearby, using a technique known as microwave holography [2–5], while the latter utilizes a TPR measuring system to determine the antenna temperature of the source.

The initial calibration consists of precision setting of the individual main reflector panels and subreflector alignment, the determination of aperture efficiency versus antenna elevation angle, and the development of a suitable pointing model to permit accurate "blind" antenna pointing. All of the measurements needed to carry out these calibrations involve far-field observations of monochromatic signals transmitted by satellite beacons, or broadband radiation from various celestial sources. Holography measurements typically are carried out at X-band (7.7 GHz) or Ku-band (12 GHz), based on the availability and elevation angle of suitable near-Earth satellite signals, while the remaining measurements utilize S-, X-, and Ka-band frequencies, depending on the equipment planned for the particular antenna under test. In all cases, some form of sampling of the source radiation as a function of antenna offset from the source is carried out, the exact nature of which, as well as the subsequent data processing, determines the precision and accuracy achieved in the overall calibration effort.

4

In the following section, we briefly describe and point out the deficiencies of the conventional approach that has been used in aperture efficiency and pointing measurements. The remainder of the article is devoted to a discussion of the approach now being pursued to significantly improve these measurements.

III. Conventional Approach to Aperture Efficiency and Pointing Measurements

To measure the gain of large antennas, one can measure the received power from a radio source that has been previously calibrated by independent means [6–8].[6] A practical method to accomplish this is to measure the received power from the calibration radio source and compare the result with the theoretical result one would measure with a "perfect" antenna. Expressed as a ratio, the result is the aperture efficiency, $\eta(\psi)$, where ψ represents the orientation of the antenna, e.g., azimuth and elevation. The formal expression for $\eta(\psi)$ is

$$\eta(\psi) = \frac{2kT_s(\psi)C_r(\psi)}{AS} \tag{1}$$

where

$$k = \text{Boltzmann's constant, } 1.38065 \times 10^{-23} \text{ W/(K-Hz)}$$
$$T_s = \text{antenna noise temperature increase due to the source, K}$$
$$C_r = \text{source-size correction factor}$$
$$A = \text{antenna aperture physical area, m}^2$$
$$S = \text{flux density of radio source, W/(m}^2\text{-Hz)}$$

The antenna aperture, A, for a circular dish of diameter d is the geometrical area, $A = \pi d^2/4$. In Eq. (1) it is assumed that the antenna points perfectly. In practice, we attribute the losses due to mispointing of the antenna separately.

While radio astronomy telescopes are designed to maximize their beam efficiency, the DSN antennas are designed for maximum aperture efficiency. Beam and aperture efficiencies are functions of the aperture illumination function. The aperture efficiency is a maximum with no taper, while the beam efficiency is a maximum with full taper. The aperture efficiency, $\eta(\psi)$, is affected by the areas of the noise shield, subreflector and strut blockages, strut shadow, amplitude taper illumination, reflector surface root-mean-square (rms) errors, and ohmic losses.

In the real world of radio astronomy, the process of measuring the antenna aperture efficiency is further complicated by the fact that sources whose radio frequency flux densities have been accurately measured tend to be rather large in angular size relative to the antenna pattern of a large-aperture radio telescope like the DSN antennas. In practice, the small angular width of the antenna beam partially resolves the angular structure of the radio source, with the result that some of the radio flux density is not collected by the antenna when it is pointed on source. A correction for source size, $C_r(\psi)$, typically is used to compensate for this effect. Note that the value of C_r is expected to vary with antenna orientation ψ because both the beam shape and the angular orientation of the radio source change as the source rises and sets across the sky.

Each of the quantities C_r and S contains a source of error, and the measurement method used to determine each must be addressed in any search for improvement. Please note that in the DSN we

---

[6] A. J. Freiley, P. D. Batelaan, and D. A. Bathker, "Absolute Flux Density Calibrations of Radio Sources at 2.3 GHz," JPL Technical Memorandum 33-806 (internal document), Jet Propulsion Laboratory, Pasadena, California, December 1, 1977.

define T at the input to the feed horn aperture and, therefore, the antenna aperture efficiency, η, is also defined at the same reference point.

A. Source-Size Correction Factor

The source-size correction factor is designed to account for the flux density of an extended source not collected by the antenna, and it is best understood with reference to the fundamental radiometric equation from which Eq. (1) is derived,

$$kT_s(\psi; \theta, \phi) = \frac{1}{2}\eta_\nu(\psi)A \iint\limits_{\text{source}} B_\nu(\theta', \phi')P_{n,\nu}(\psi; \theta' - \theta, \phi' - \phi)d\Omega' \tag{2}$$

where B_ν is the source brightness function, $P_{n,\nu}$ is the normalized antenna power pattern, and (θ, ϕ) are rectangular, angular coordinates relative to the source center [9].[7] Here, we have been specific regarding the dependence of various quantities on the antenna pointing direction, ψ, and the operating frequency, ν, as well as the fact that the measured system noise temperature increase due to the source, T_s, depends on the antenna pointing.

The integral appearing in Eq. (2) is the source flux density collected by the antenna, and it is smaller than the total source flux density emitted by the source,

$$S_\nu = \iint\limits_{\text{source}} B_\nu(\theta, \phi)d\Omega \tag{3}$$

unless the source is much smaller in extent than the antenna main beam and the antenna is accurately pointed at the source. Equation (2) may be cast into the form of Eq. (1) by defining the source-size correction factor,

$$C_{r,\nu}(\psi, \theta_m, \phi_m) = \frac{S_\nu}{S_{\text{coll},\nu}(\psi, \theta_m, \phi_m)} \geq 1 \tag{4}$$

where

$$S_{\text{coll},\nu}(\psi)|_{\text{max}} = S_{\text{coll},\nu}(\psi, \theta_m, \phi_m) = \iint\limits_{\text{source}} B_\nu(\theta', \phi')P_{n,\nu}(\psi; \theta' - \theta_m, \phi' - \phi_m)d\Omega' \tag{5}$$

is the *maximum* flux density collected by the antenna, i.e., the antenna noise temperature field, $T_\nu(\psi; \theta, \phi)$, must be explored at a given elevation angle until the maximum value corresponding to the coordinates (θ_m, ϕ_m) is found. It should be noted that these coordinates will not be those for the source center unless the source happens to be symmetric.

Equations (4) and (5) imply that the determination of $C_{r,\nu}(\psi, \theta_m, \phi_m)$ requires a knowledge of the source brightness function and the normalized antenna power pattern. For those circumstances where $C_{r,\nu}(\psi)$ is within a few percent of 1, the usual approach to its evaluation has been to estimate both of these functions by symmetric Gaussians, in which case one obtains the oft-quoted formula

---

[7] P. Richter, *Radio Source List for Antenna Calibration*, JPL D-3801, DSN 890-269 (internal document), Jet Propulsion Laboratory, Pasadena, California, October 15, 1994.

$$C_{r,\nu} = 1 + \left(\frac{\Theta_S}{\Theta_B}\right)^2 \tag{6}$$

where Θ_S and Θ_B are the source and antenna beam widths, respectively. For a disk-like distribution, on the other hand, the correction factor is

$$C_{r,\nu} = \left[\frac{(1 - e^{-x^2})}{x^2}\right]^{-1} \tag{7}$$

where

$$x = (4\ln 2)^{1/2} * \frac{R}{\Theta_B} \tag{8}$$

and R is the angular radius of the disk [10].

However, many commonly used sources have corrections approaching 100 percent for a large antenna operated at high frequency. The source-size correction value for Virgo A, at Ka-band, on the 70-m antenna, for example, is calculated to be 1.90. At S-band, the value for the source-size correction for the same source on the 70-m antenna is 1.205.[8] Under these circumstances, the computation of the source-size correction must be carried out with more realistic functional representations of the source structure, and the source of these has been brightness maps measured with very long baseline interferometry (VLBI) arrays or large antennas such as the 100-m antenna at Bonn, Germany.

It is possible, in principle, to carry out a proper deconvolution of such maps to compute Eq. (5). Thus, an average brightness map is obtained with an antenna having an equivalent normalized far-field power pattern, $P_{0,n}(\theta, \phi)$, which is given by

$$B_0(\theta, \phi) = \frac{1}{\Omega_0} \iint\limits_{\text{source}} B(\theta', \phi') P_{0n}(\theta - \theta', \phi - \phi') d\Omega' \tag{9}$$

where Ω_0 is the equivalent measuring beam solid angle, and we now drop the explicit frequency and elevation angle notation and for simplicity assume beam symmetry so that the integral has the form of a convolution. Then, taking the Fourier transform of Eqs. (5) and (9), we have

$$\tilde{S}(\mu, \nu) = \tilde{B}(\mu, \nu)\tilde{P}_n(\mu, \nu)$$

$$\tilde{B}_0(\mu, \nu) = \frac{1}{\Omega_0}\tilde{B}(\mu, \nu)\tilde{P}_{0n}(\mu, \nu) \tag{10}$$

from which we obtain

$$\tilde{S}(\mu, \nu) = \Omega_0 \frac{\tilde{P}_n(\mu, \nu)}{\tilde{P}_{0n}(\mu, \nu)} \tilde{B}_0(\mu, \nu) \tag{11}$$

---

[8] Ibid.

so that performing the inverse Fourier transform yields $S_{\text{coll}}(\theta, \phi)$ from which $S_{\text{coll}}(\theta_m, \phi_m)$ may be found. In the above, μ, ν are the spatial frequency coordinates. This procedure has in fact been used to generate the C_r values currently used in the DSN for calibration purposes [10],[9] but the approach has a number of limitations that become serious at high frequencies:

(1) Maps are usually not available at the frequency of interest, so an interpolation procedure must be used to estimate a map at the required frequency.

(2) Large antennas have significant flexure as a function of elevation angle due to gravitational loading, resulting in aberrations that affect the beam pattern, so that the values of C_r ought to be calculated as a function of elevation angle; see Eq. (4).

(3) Information on the mapping beam solid angle and shape is often approximate or unavailable in the literature.

Thus, an alternative approach that eliminates the need for source-size corrections is called for, and this approach is described in a following section.

B. Flux Density

Since source flux densities are determined from the same equation used to determine aperture efficiency, Eq. (1), all of the sources of error attendant on the latter must apply to the former as well. Thus, while the very brightest sources can be measured with a low-gain system such as a horn, whose calibration is relatively straightforward, the transfer of information from strong to weak sources, which are compact enough to serve as reasonable calibrators for large antennas, must be carried out with larger antennas. Then, Eq. (1) leads to the result

$$\frac{S_1}{S_2} = \frac{T_1}{T_2}\frac{C_{r1}}{C_{r2}} \tag{12}$$

where the subscripts refer to measurements of two different sources with the same antenna, and we see that not only antenna temperatures, but also source-size corrections, enter into the calculation of flux density ratios for different sources.

A survey of the literature on flux density measurements shows that the use of inaccurate C_r values contributes significantly to the error budget for such measurements [7,10],[10,11] so that eliminating the need for such a correction would result in a significant increase in the accuracy of flux density determinations.

C. Source Temperature

The basic method for measuring the system noise temperature increase due to a source involves some form of on-source, off-source subtraction. In the conventional approach, sometimes termed "autobore," this is accomplished by a boresight technique in which the antenna is successively offset in a given direction, say θ, relative to the source by ± 5, $\pm 1/2$, and 0 antenna half-power beamwidths (HPBWs). The resulting 5 data points then are fitted to a Gaussian function plus a linear background to account for the decrease in system noise temperature with elevation angle, and from this fit, the maximum, or peak source noise temperature, and θ pointing error and beamwidth are determined. This pointing error is then used to execute an orthogonal boresight in the ϕ direction, and the process is repeated as the source is tracked.

---

[9] Ibid.

[10] A. J. Freiley et al., op cit.

[11] P. Richter, op cit.

While this works well at S-band, it is less satisfactory at X-band, and is unsatisfactory at Ka-band, especially with regard to the pointing determination, where, for example, it has been unable to provide the requisite precision to meet the radio science requirements for the Cassini mission to Saturn.[12] Additionally, the method is inherently slow since each of the 5 measurements in a given direction requires that the antenna servos and mechanical structure settle at the offset specified before a noise temperature measurement is made. A further problem is that the Gaussian fitting function only approximates the actual profile of the noise temperature measurement which follows the antenna far-field pattern function, and for an extended source this approximation may not be very good.

In view of these limitations, one would like to have a source noise temperature measurement of inherently greater accuracy. This would not only improve our knowledge of antenna gain and pointing, but would also improve the calibration of weak sources by the comparison method described above. In the following section, we describe a new approach to the calibration of large, ground-based antennas that significantly improves the precision achieved by reducing or eliminating the above-noted sources of error inherent with present methods.

IV. The Raster-Scan Method

The key to reducing the error sources discussed in the previous section lies in making system noise temperature measurements over a finite area of sky including the source, rather than along orthogonal cuts through the temperature profile. Thus, integration of Eq. (2) over the two-dimensional (2-D) angular field (θ, ϕ) gives

$$
k \iint_{\substack{\text{source} \\ +\text{beam}}} T_S(\theta, \phi) d\Omega = \frac{1}{2} \eta A \Omega S
\tag{13}
$$

where Ω is the antenna beam solid angle, and we have dropped the explicit frequency and elevation angle notation for simplicity.

If we now consider the application of the above equation to two sources, the equivalent of Eq. (12) becomes

$$
\frac{\iint\limits_{\substack{\text{source} \\ +\text{beam}}} T_1(\theta, \phi) d\Omega}{\iint\limits_{\substack{\text{source} \\ +\text{beam}}} T_2(\theta, \phi) d\Omega} = \frac{S_1}{S_2}
\tag{14}
$$

a result independent of source-size corrections.

If the source considered in Eq. (13) is small enough relative to the main beam to be considered a point, then its brightness may be represented by

$$
B(\theta, \phi) = S_P \delta(\theta) \delta(\phi)
\tag{15}
$$

where $\delta(x)$ is the Dirac delta function. Then, Eqs. (4) and (5) show that $C_r = 1$ so that Eq. (1) becomes

---

[12] M. Adler, *Cassini Project Policies and Documents*, Rev. D, JPL D-9945 (internal document), Jet Propulsion Laboratory, Pasadena, California, 1995.

$$\eta = \frac{2kT_P}{AS_P} \tag{16}$$

If the flux density, S_p, of this point source is known, then Eq. (16) immediately yields the aperture efficiency in terms of the peak source temperature. However, it frequently is the case that point sources bright enough for calibration purposes are also variable, so that one may not have a priori knowledge of S_p. In this case, Eq. (14) may be used to determine S_p by comparison with an extended, calibrated source whose flux density, S_c, is known. Then, combining Eqs. (14) and (16), we have

$$\eta = \frac{2kT_P}{AS_C} \frac{\iint T_c(\theta, \phi)d\Omega}{\iint T_p(\theta, \phi)d\Omega} \tag{17}$$

which now becomes the fundamental equation for determining aperture efficiency. These equations can now be arranged to solve for the source-size corrections as follows:

$$C_r(\psi, \theta_m, \phi_m) = \frac{S_c}{S_p} = \frac{T_p(\theta_m, \phi_m)}{T_c(\theta_m, \phi_m)} \frac{\iint T_c(\psi, \theta, \phi)d\Omega}{\iint T_p(\psi, \theta, \phi)d\Omega} \tag{18}$$

The data for the computation implied by Eqs. (17) and (18) are the temperature fields $T_P(\theta, \phi)$ and $T_C(\theta, \phi)$ for the point and extended calibration sources, respectively, and these are obtained by scanning the antenna beam across the source in a raster pattern, similar to a (non-interlaced) television scan (Fig. 4). All the terms on the right side of Eq. (17) are either known values or are measured by the OTF-mapping system.

It should be noted here that the ratio of the integrals appearing in Eqs. (17) and (18) is, by Eq. (14), just the ratio of the flux densities for the two sources, i.e., a constant. Thus, the measurement strategy should involve the alternate scanning of the two sources over a small but finite elevation change so that the data points corresponding to each integral, as a function of elevation, can be fitted to a linear, or perhaps quadratic, function. Then, it should be found that the ratio of these two fitting functions is constant and equal to S_C/S_P. These results illustrate some of the valuable features of the OTF-mapping system:

(1) The need to derive source-size correction factor $C_r(\psi)$ is eliminated. However, one has the option to calculate $C_r(\psi)$ for various calibration radio sources using Eq. (18).

(2) The need to derive accurate values of T_c for extended sources is eliminated. This is desirable because accurate derivations of T_c require mapping and deconvolving source structure from the antenna patterns which change with antenna orientation (ψ). Using the OTF-mapping technique, the accuracy of the antenna efficiency measurement is limited by the accuracy with which the calibration source flux density S_c is known.

(3) The OTF-mapping system enables the experimenter to use compact point-like sources as secondary calibration sources for precision antenna calibrations. The vast majority of these radio sources are quasars, which are so distant that their angular sizes are very small. The problem is their radio brightness (flux density) values are highly variable, so one must calibrate them against the handful of absolutely calibrated radio sources that are available. With few exceptions, the time scales of the quasar variations are typically a few days, so flux density calibration measurements can be done rather infrequently and relative measurements of antenna performance with azimuth and elevation can be done almost any time.
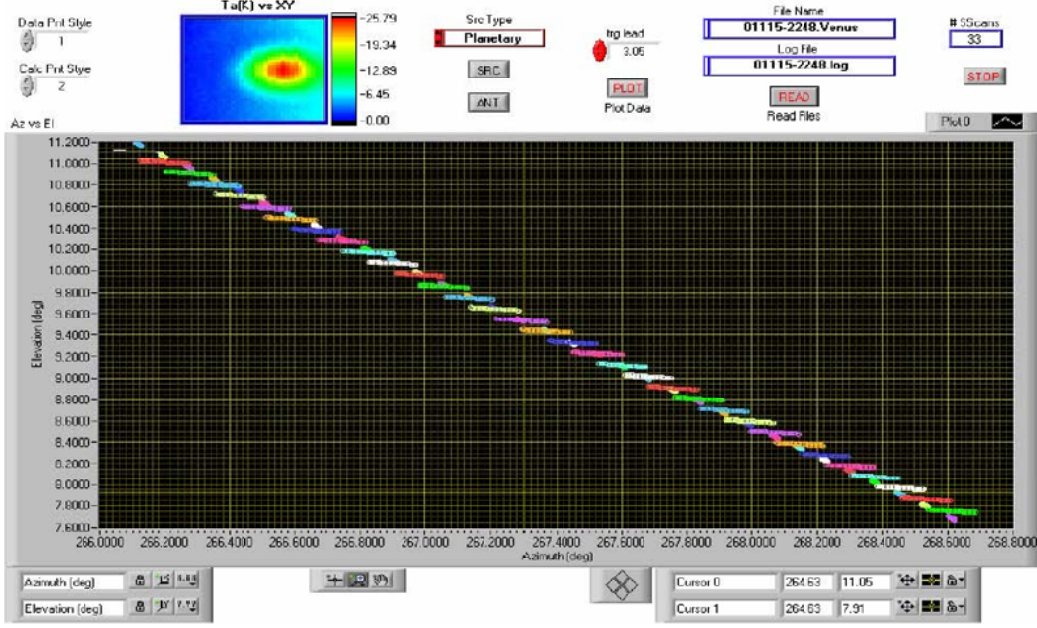
Fig. 4. A raster scan performed at 13.8 GHz by the TPR, creating a 33 x 33 image of Venus as it sets. The raster scan is designed to image the planet at the center of the image. The deviation of the image position from the center is the result of pointing errors introduced by the antenna combined with difficult refraction correction computations at the low-elevation angle of 7.6 deg. The color dots above and below the scans are the computed observation coordinate of the source at the mid-point of each scan. The combined data from the 33 scans are then displayed above.

As a practical matter, the extended calibration source 3c274 (Virgo A) and the variable point source 3c273 serve admirably for such a strategy as they have nearly the same right ascension.

Substitution of Eq. (15) into Eq. (2) gives the result

$$T_P(\theta, \phi) = \frac{\eta A S_P}{2k} P_n(\theta, \phi) = T_P P_n(\theta, \phi) \tag{19}$$

so that the raster scan data set for the point source has a functional dependence determined by the beam pattern plus a background term due to the sky, which may be linearly approximated over the small field scanned. Thus, if we assume that the antenna is in good alignment, there are small system aberrations, and the main reflector is nearly uniformly illuminated, which is a good approximation for the shaped reflector designs of the DSN. Then $P_n(\theta, \phi)$ can be well-approximated by an asymmetric Airy pattern

$$A(\kappa_\theta \theta, \kappa_\phi \phi) = \left[\frac{2 J_1 \sqrt{\kappa_\theta^2 \theta^2 + \kappa_\phi^2 \phi^2}}{\sqrt{\kappa_\theta^2 \theta^2 + \kappa_\phi^2 \phi^2}} \right]^2 \tag{20}$$

so that the system temperature data set for the point source raster scan has the form

$$T_{\mathrm{op}}(\theta, \phi) = T_P A\big[\kappa_\theta(\theta - \theta_0), \kappa_\phi(\phi - \phi_0)\big] + T_{\mathrm{op}} + a_\theta \theta + a_\phi \phi \tag{21}$$

where κ_θ and κ_ϕ are beamwidth parameters, θ_0 and ϕ_0 are the pointing errors, a_θ and a_ϕ are the sky background coefficients for the θ and ϕ directions, and T_{op} is the system operating noise temperature.

11

The 8 parameters appearing in Eq. (21) may be found from a nonlinear, least-squares fit to the point source raster scan data, thus giving complete information on the peak temperature, and pointing errors and beamwidths for the two orthogonal directions corresponding to the scan axes. The precision of the resulting fit depends on the noise fluctuations present in the noise temperature data, the scan parameters, and the data processing used, and these are dealt with in the following sections [11].

A. Fluctuations in System Noise Temperature

Three main sources of fluctuation of system noise temperature can be identified:

(1) Thermal noise generated in the radiometer and atmosphere.

(2) Gain-bandwidth variations in the radiometer caused by ambient temperature fluctuations of electronic components, especially in the first stages.

(3) Fluctuations caused by variations in tropospheric density, especially of water vapor content. This is most significant at Ka-band.

In order to characterize and model the performance of the TPR, the two-sided power spectral density (PSD) was measured. The output fluctuations of a typical DSN Ka-band radiometer have been measured as a function of fluctuation frequency over the range from 6.5×10^{-5} to 0.5 Hz, and the results compared with a model based on the above mechanisms. The results are shown in Fig. 5, where curve (a) corresponds to the radiometer looking at an ambient load and curve (b) was obtained with it looking at the zenith sky. Curve (c) is a fit to curve (a) decreased by the square of the ratio of the system operating noise temperatures, $T_{\mathrm{op}}|_{\mathrm{amb}} / T_{\mathrm{op}}|_{\mathrm{sky}} \cong 14.6$, and curve (d) corresponds to a statistical model for tropospheric fluctuations for average conditions at the DSN complex at Goldstone, California [12]. Curve (a), which is constant at high frequencies and follows a $1/f^2$ dependence at low frequencies, corresponds to thermal noise and gain-bandwidth variations, and if these were the only terms present with the radiometer looking at the zenith sky, the data of curve (b) would follow curve (c). There is a significant departure from this, however, but when curves (c) and (d) are added together the result follows curve (b) closely, from which we conclude that tropospheric fluctuations play an important role in the total radiometer fluctuations at frequencies below about 0.1 Hz.
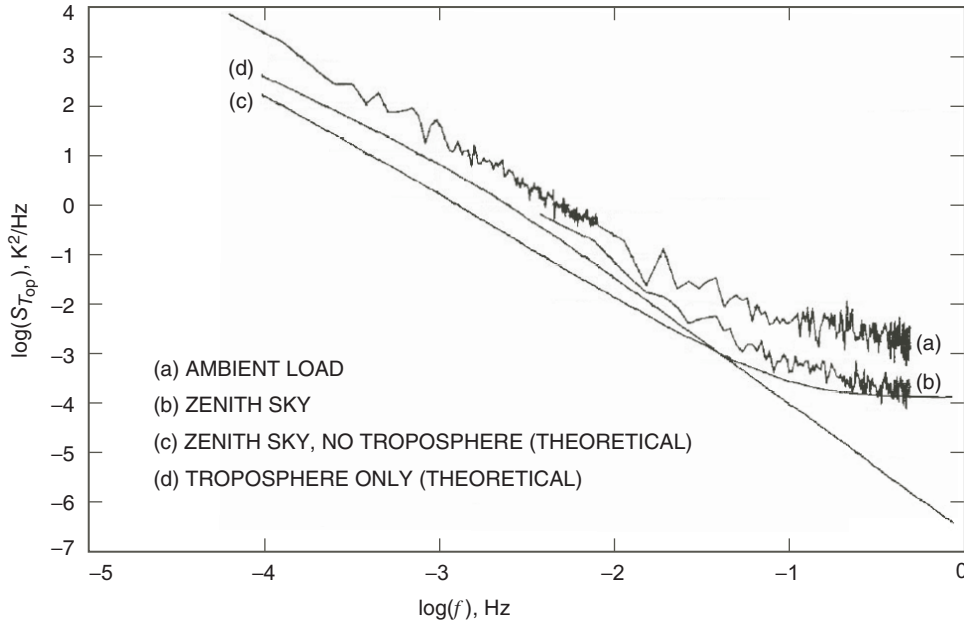

Fig. 5. Two-sided PSD of T_{op} fluctuations for a Ka-band radiometer.

Since we are interested in frequencies greater than 10^{-3} Hz when making gain calibrations, i.e., the times of interest are considerably shorter than 1000 s, we may consider only the high frequency behavior of the Treuhaft–Lanyi model, which has a $1/f^{8/3}$ dependence so that curve (b) may be represented by the equation

$$S_{T_{\text{op}}}(f) = S_0 + \frac{K_1}{f^2} + \frac{K_2}{f^{8/3}} \tag{22}$$

where the coefficients for the Ka-band radiometer tested have the values

$$S_0 = 1.50 \times 10^{-4} \text{ K}^2/\text{Hz}$$

$$K_1 = 1.64 \times 10^{-6} \text{ K}^2/\text{s}$$

$$K_2 = 2.36 \times 10^{-7} \text{ K}^2/\text{s}^{5/3}$$

corresponding to average weather with the radiometer looking at the zenith sky, and a T_{op} of approximately 100 K.

With the above form for the PSD of the fluctuations, one may determine the corresponding standard deviation of the fluctuations. This depends on the system operating temperature, T_{op}; the RF system bandwidth, B; the integration time, τ, used during the measurements; and, in view of the nonstationary behavior indicated by Eq. (22), the total duration of the measurement, T. It can be shown that the variance of a random process $X(t)$, of duration T, having a high frequency cutoff, is given by

$$\sigma_X^2(\text{T}) = 2 \int_0^\infty \left[1 - \text{sinc}^2(\pi f \text{T})\right] S_X(f) df \tag{23}$$

where $\text{sinc}(x) = \sin(x)/x$, and $S_X(f)$ is the two-sided PSD of the process. If the $X(t)$ signal is continuously averaged over a time interval τ, the resulting PSD is

$$S_{\bar{X}}(f) = \text{sinc}^2(\pi f \tau) S_X(f) \tag{24}$$

so that the variance of the averaged process $\bar{T}_{\text{op}}(t)$, of duration T, is

$$\sigma_{\bar{T}_{\text{op}}}^2(\tau, \text{T}) = 2 \int_0^\infty \left[1 - \text{sinc}^2(\pi f \text{T})\right] \text{sinc}^2(\pi f \tau) S_{T_{\text{op}}}(f) df \tag{25}$$

The evaluation of this integral for the spectrum given by Eq. (22) is accomplished by contour integration, with the result

$$\sigma_{\bar{T}_{\text{op}}}(\tau, \text{T}) = \sqrt{\frac{S_0}{\tau} + \frac{2\pi^2 K_1}{3}\text{T} + 18.3 K_2 \text{T}^{5/3}} \tag{26}$$

where it has been assumed that the measurement duration is considerably longer than the integration time, i.e., $\text{T} \gg \tau$.

The duration of the measurement of interest in the raster scan method depends on the rate at which the data are taken and the details of the analysis. For example, if one were to operate at a lower frequency than Ka-band, the $T^{5/3}$ term in the above equation, corresponding to tropospheric fluctuations, would be absent, and if a radiometer gain calibration were carried out at the conclusion of each line of the scan, then the appropriate time would be the time required for the execution of a single scan line. Generally speaking, however, T will be the time required for one complete raster, and an important conclusion to be drawn from Eq. (26) is the need for *short* measurement times. This perhaps counterintuitive conclusion has been born out in actual tests, as will be shown below.

B. OTF-Mapping Research and Development System Design

The analysis carried out in Sections III and IV, culminating in Eq. (17) expressing the aperture efficiency, η, as a function of the source temperature of a point source, demonstrates that the raster scan geometry and timing should be determined primarily by the need to accurately derive this quantity, T_p, and this question is discussed in what follows.

Equation (26), together with the need to avoid settling problems with the antenna mechanical system, suggest that the raster scan should be performed with a continuous motion at a constant, high angular velocity in a given direction, say θ, while discontinuously stepping in the orthogonal direction, again mimicking a television scan (Fig. 4). This means that the data are taken "on the fly," hence the term "OTF-mapping." In so doing, the averaging process referred to above will contribute to a distortion of the signal that must be taken into account.

A second and related consideration is selection of the sampling interval t_s. In view of the Fourier transform relationship between the complex, far-field amplitude, $U_n(\theta, \phi)$, and the complex aperture field, $G(x, y)$, the scan signal for a single line of a point source is absolutely bandlimited. Thus, for a coherent detection scheme such as that used in the microwave holography system [3–5,16], which also uses a raster scan format, the signal is of the form $VU_n(\dot{\theta}t, \phi)$, where V is an arbitrary amplitude factor related to the antenna gain and $\dot{\theta} = d\theta/dt$ is the constant scan angular velocity. The spectrum of this signal has, by virtue of the clearly defined antenna aperture, a sharp cutoff at $f_0 = \dot{\theta}/2\Theta_B$, where $\Theta_B = \lambda/2a$ is approximately equal to antenna main beamwidth. This cutoff, moreover, is independent of the main reflector shape, illumination, and system aberrations, and depends only on the maximum dimension of the aperture, d, in the scanned direction.

Similarly, for the noncoherent (TPR) detection used in gain measurements, the signal is of the form

$$VP_n(\dot{\theta}t, \phi) = V \left| U_n(\dot{\theta}t, \phi) \right|^2 \tag{27}$$

so that its spectrum is given by the autocorrelation of the coherent spectrum, and it consequently has a cutoff frequency twice as high.

From the above, we infer that Nyquist sampling for a coherent system requires a minimum of one sample per beamwidth, while for a noncoherent system, a minimum of two samples per beamwidth is required. Also, since the signal spectrum is bandlimited in both cases, a sharp cutoff digital filter can be used to remove noise above the cutoff, and this can then be followed by a suitable Wiener filter to compensate for the distortion introduced by the integration, with minimal loss of high-frequency information.

Figure 6 shows a schematic diagram of the antenna calibration OTF-mapping research and development (R&D) system. It can calibrate any of the DSN antennas by means of interfaces to their antenna controller, encoder read outs, and diodes and microwave controls. All the interfaces must be done locally at the antenna under test. The system achieves high accuracy of raster alignments by virtue of interfaces to the antenna angle encoders, which are being read at a high speed of 1000 readings/s. An internal computation
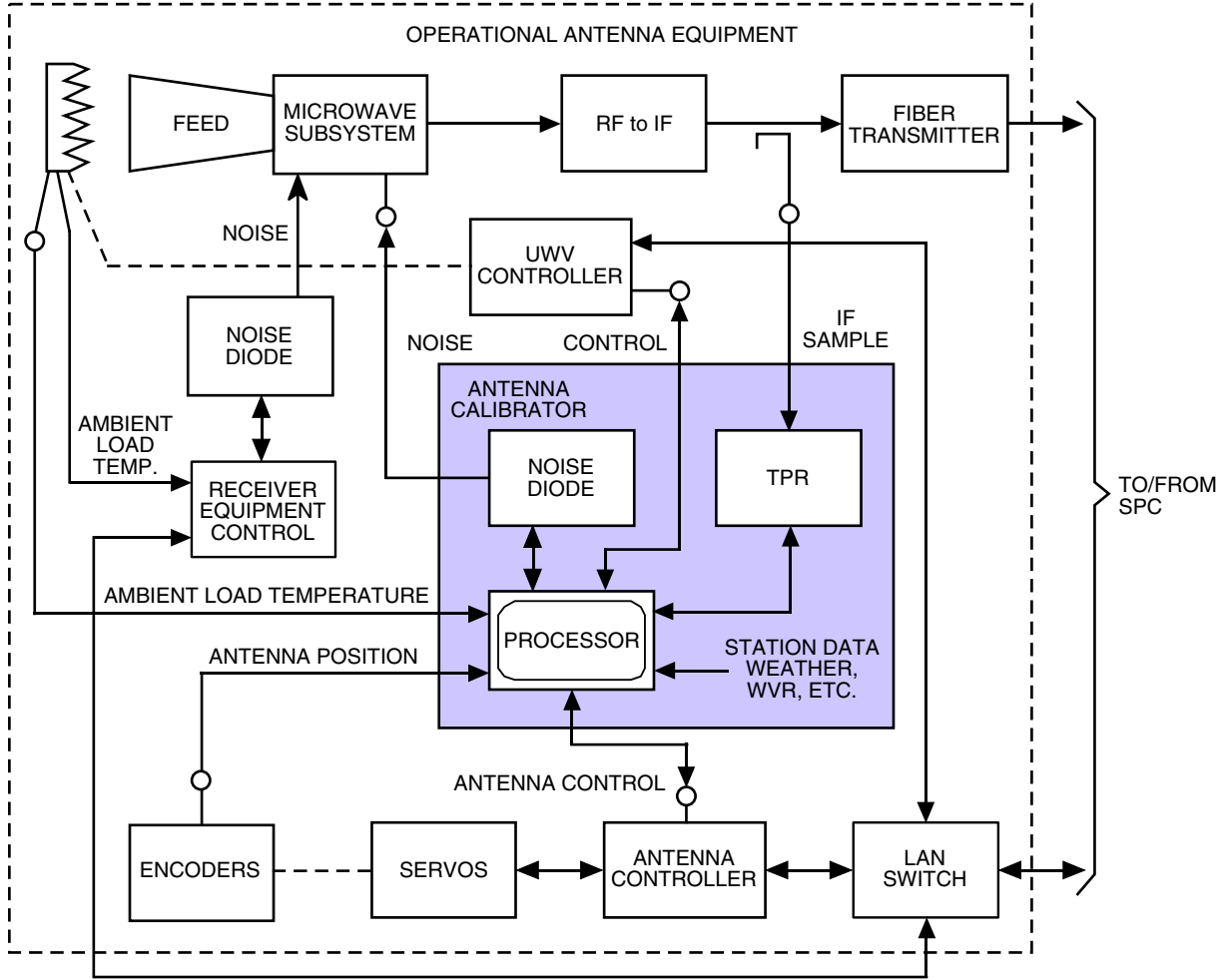
Fig. 6. OTF-mapping (raster scan) R&D system, in the shaded area, showing interfaces to any DSN antenna.

engine in the data acquisition converts the sidereal motion of radio sources from right ascension–declination (RA-DEC) to antenna coordinates in azimuth–elevation (AZ-EL) in real time, allowing for a tight feedback loop control of synchronizing the receiver triggering (TPR) to the antenna position.

The first trigger position in each of the raster subscans is determined by position synchronization, while the remaining data are triggered by means of time synchronization locked to the internal system clock. As a result, one of the critical elements of this design is the need to maintain a constant, known angular velocity of antenna motion during the taking of data along a given direction. The TPR is sampled at a constant known rate so that the relative position at which the data are taken is known with high accuracy and antenna-settling time is no longer an issue. This design ensures the alignment of the individual subscans within the full raster. The OTF-mapping R&D data acquisition algorithms include the computation of the radio source positions such that at any given time the position of the antenna relative to the source is known. Since the data are taken on the fly, the integration occurring during the sampling interval results in an attenuation of high-frequency information (smearing), but this can be recovered by an inverse filtering process (Wiener filter). The source is scanned in a raster-type pattern by stepping from line to line, so that a complete data set corresponding to a complete raster contains all of the relevant data and not just a sampling of it along two orthogonal directions. This means that one is effectively including all of the source radiation so that no source-size correction is necessary [Eqs. (17)

and (18)]. The resulting 2-D data set is then used to determine, by means of least-squares fitting, the best-fit main-beam pattern, from which the relevant calibration parameters are directly determined. Figures 7 and 8 show the real-time display of the OTF-mapping R&D data acquisition instrumentation display for the one-dimensional (1-D) and 2-D cases, respectively.

In both cases, Eqs. (20) and (21) are solved using the Levenberg–Marquardt method to determine the nonlinear set of coefficients of these equations which minimize a chi-square quantity. In Fig. 7, the white dots are the raw data, and the red line is the fitting Airy function. Figure 8 shows the real-time display during the acquisition of a 2-D raster (middle color plot) while individual subscans are shown above in a white over black plot. In both cases, the precision in the estimation of the equation parameters is determined from the diagonal elements of the covariance matrix and is also displayed in real time for parameters of interests. Figure 9 shows the main program panel of the OTF-mapping R&D system.

In order to study the interaction between scan velocity, $\dot{\theta}$, array size, N, and integration time, τ, computations have been made of the errors expected in the fitted parameter T_p for a range of values for each of these parameters for a one-dimensional fit corresponding to a single scan line, and the results are shown in Table 1. The rms background noise from a single scan line, σ_l, and complete raster, σ_r, is computed for a given scan line duration, t_l, and raster duration, t_r, from a model based on the measured power spectral density for the radiometer system. In all cases, the sampling interval is $t_s = \tau/2$. The computed errors in T_p are based on a general, nonlinear least-squares fitting analysis, using Eq. (26) to estimate the noise standard deviation and a Gaussian beam pattern rather than an Airy pattern for simplicity.

Also shown in Table 1 are the rms fitting errors of aperture efficiency versus elevation curves based on quadratic fits to the data for a complete 6 hour pass of the source. These errors are inversely proportional to $\sqrt{N_r}$, where N_r is the number of complete rasters executed during the pass, each of which yields an estimate of all of the fitting parameters:

$$T_P(\theta) = T_P \exp\left[\frac{-\kappa_\theta^2(\theta - \theta_0)^2}{2}\right] \tag{28}$$
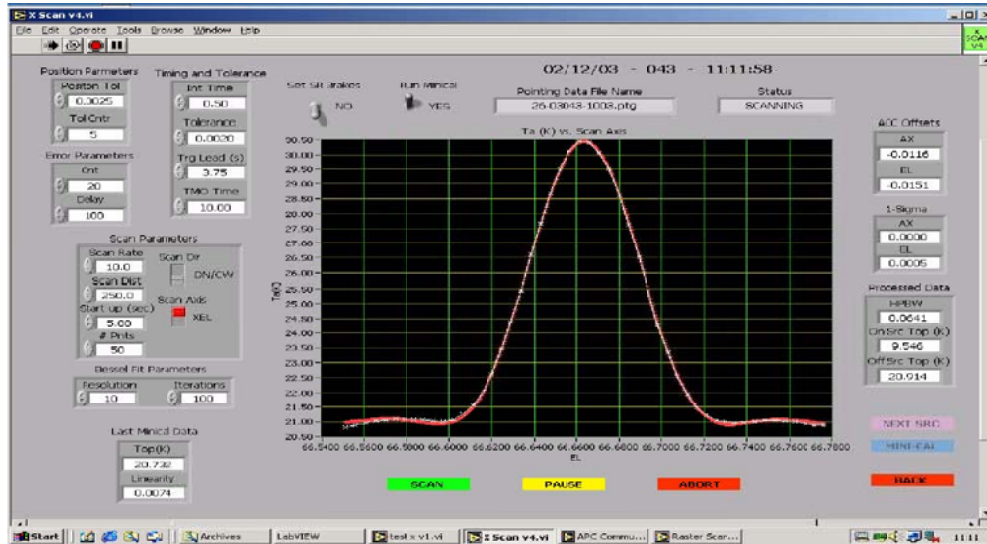

Fig. 7. OTF-mapping R&D data acquisition real-time display.
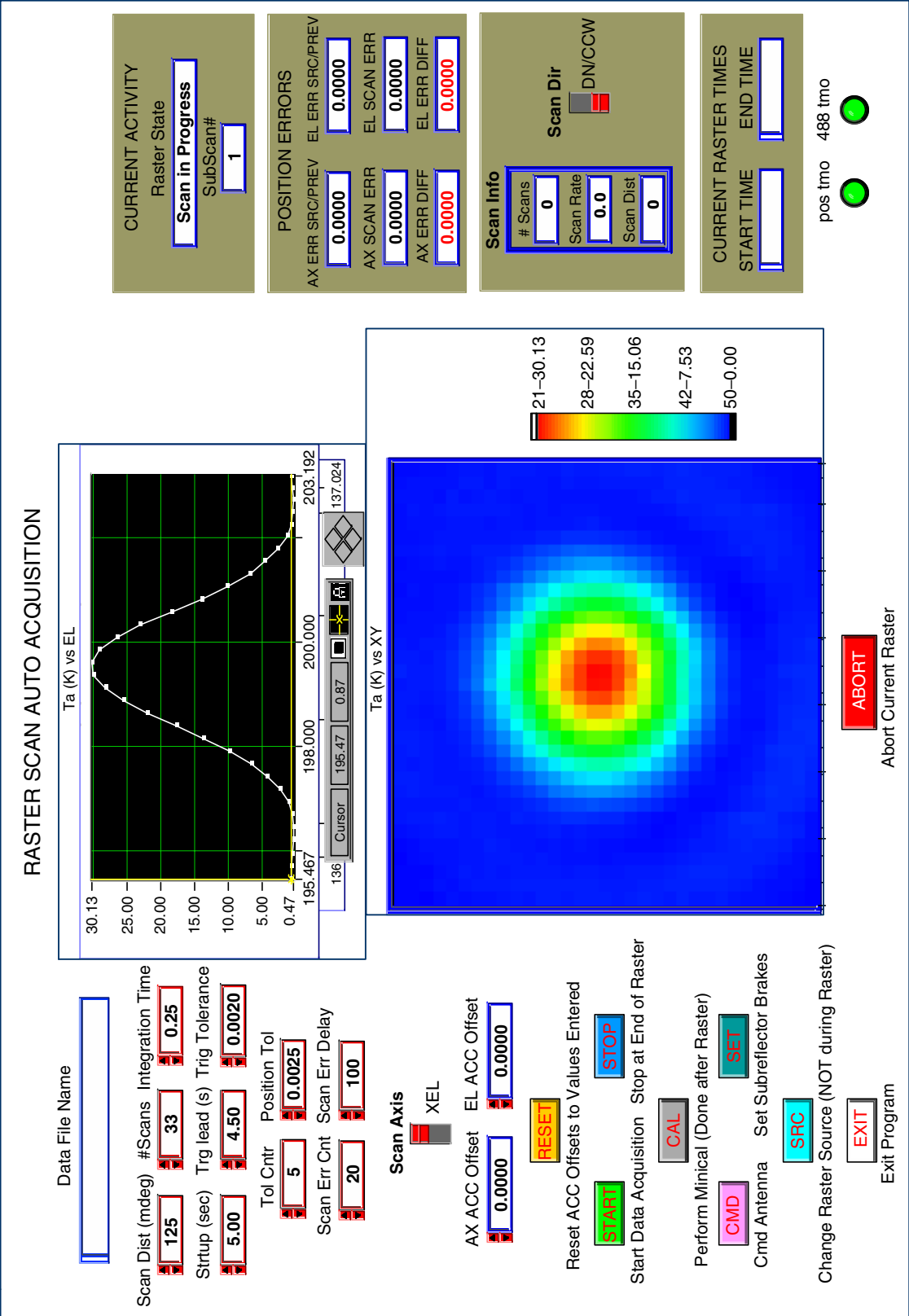
16

Fig. 8. Real-time display of the OTF-mapping R&D instrumentation during the acquisition of a 2-D raster.
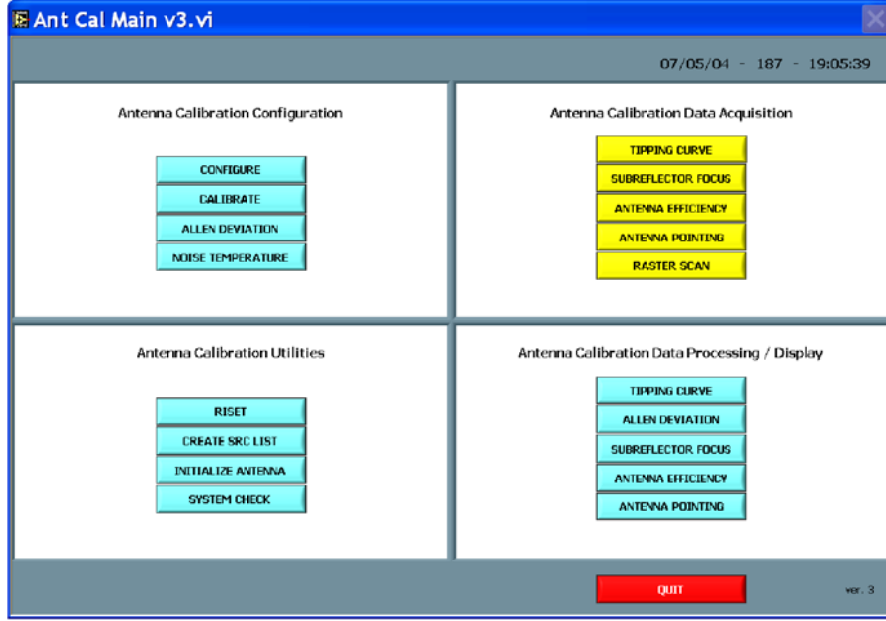
Fig. 9. OTF-mapping R&D main program panel.

Table 1. Theoretical simulation errors for the source temperature, and aperture efficiency $\eta(\psi)$ versus elevation curve, as a function of the scan velocity, array size, *N*, based on nonlinear least-squares fitting analysis for raster scan data acquired with a 34-m antenna at Ka-band (elevation = 90 deg, with troposphere, retrace time = 2 s).

τ, s	t_l, s	t_r, s	$\dot{\theta}$, mdeg/s	σ_l, K	σ_r, K	σ_T, K	$\overline{\sigma}_{\mathrm{FIT}}$, percent	N_r
				$N = 17$				
0.1	0.8	47.6	100	0.036	0.068	0.037	0.042	453
0.2	1.6	61.2	50	0.026	0.074	0.041	0.052	352
0.4	3.2	88.4	25	0.019	0.094	0.052	0.080	244
0.8	6.4	142.8	12.5	0.017	0.136	0.075	0.147	151
1.6	12.8	251.6	6.24	0.022	0.214	0.118	0.309	85
				$N = 33$				
0.1	1.6	118.8	50	0.037	0.123	0.034	0.060	181
0.2	3.2	171.6	25	0.027	0.159	0.044	0.095	125
0.4	6.4	277.2	12.5	0.026	0.232	0.064	0.176	77
0.8	12.8	488.4	6.24	0.024	0.369	0.101	0.370	44
				$N = 65$				
0.1	3.2	338.0	25	0.038	0.275	0.038	0.115	63
0.2	6.4	546.0	12.5	0.029	0.405	0.055	0.215	39

18

V. Test Results

A. OTF-Mapping Test Results

Field test results agree very closely with the computed performance predictions presented in Table 1. As a typical example, an observation of Venus has the following parameters (see Fig. 10):

$$\text{Source} = \text{Venus}$$

$$\text{Raster size} = 33 \times 33$$

$$\text{Total measurement distances} = 125 \times 125 \text{ mdeg}$$

$$\tau = 0.25 \text{ s}$$

$$\text{Scan velocity} = 15.6 \text{ mdeg/s}$$

$$\text{Total measurement duration} = 430 \text{ s}$$

$$\text{Encoder sampling rate} = 1000/\text{s}$$

$$\text{TPR sampling rate} = 150/\text{s}$$

The peak temperature was obtained by fitting the data to a 2-D Airy function, which resulted in a 1-sigma error of 0.085 K. This result is very much in agreement with the predictions computed in Table 1.

The system also computes the reduced chi-square such that, if high values are computed, it can be concluded that a main source of the error is due to the fact that the fitting function cannot follow the data to within the limit imposed by the random data errors. In field measurements, we found out that indeed this is the case when the antenna side lobes are asymmetric, as they would be due to poor subreflector alignment.
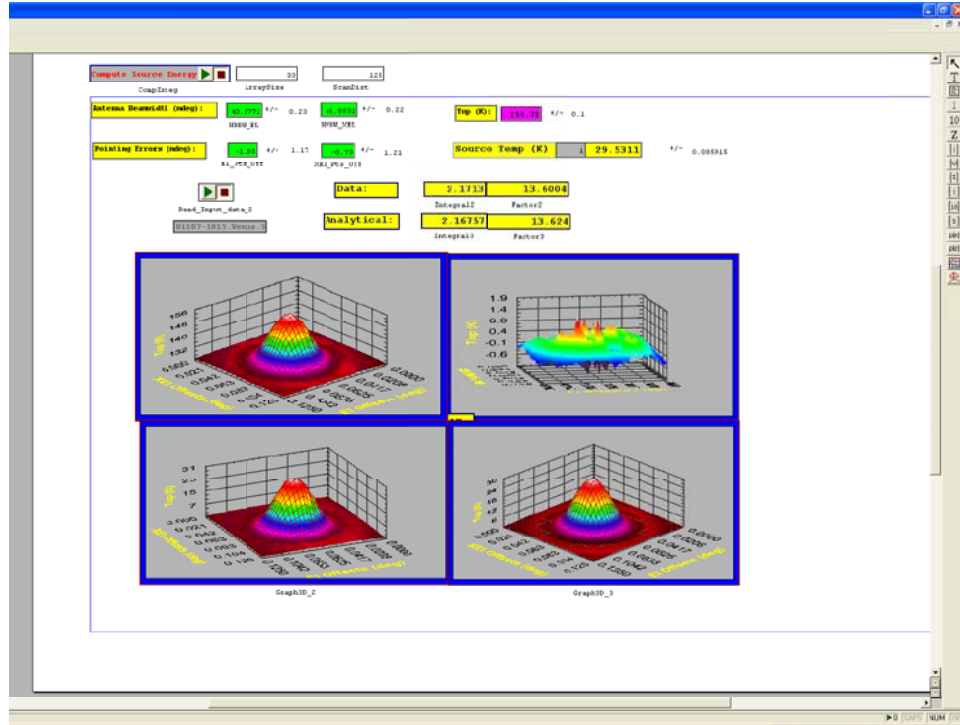
Fig. 10. A screen capture of an error analysis for a full 2-D raster scan indicates that an accuracy of 0.1 K was achieved in determining the source peak temperature: top left, raw data; bottom left, raw data after removal of background and slope; bottom right, fitting function to raw data on the bottom left; and top right, map differencing between the raw data and fitting function.

B. Blind-Pointing Calibration Test Results

The OTF-mapping R&D system also proved itself capable of providing a new record of best blind-pointing performance, which was achieved on the DSN 34-m BWG antennas. In doing so, two new technologies were used:

(1) The OTF-mapping R&D system [13]

(2) The new fourth-order pointing model software [14][13]

The fourth-order pointing model was devised as a result of noticing systematic error residuals remaining in the data after applying the conventional first-order model. The first-order model, which typically has 6 to 8 mathematical terms (Fig. 11), is a physical model originally developed by Peter Stumpff [22]. The fourth-order model (Fig. 12) was derived by expanding the spherical harmonics, which are related to the associated Legendre polynomials by Eqs. (29) and (30), to the fourth order, resulting in 59 mathematical terms:

$$Y_{lm}(\theta, \phi) = \sqrt{\frac{2l + 1(l - m)!}{4\pi(l + m)!}} P_l^m \cos(\theta) e^{im\phi} \tag{29}$$

where

$$P_l^m(x) = (-1)^m (1 - x^2)^{m/2} \frac{d^m}{dx^m} P_l(x) \tag{30}$$

All the physical terms from the first-order model that did not appear in the expansion were retained in the new model. As shown in Figs. 11 and 12, the application of the new fourth-order model reduces the mean radial error (MRE) by a factor of approximately 2. Additional field tests confirmed that the blind-pointing performance improved by approximately a factor of 2 to 3 relative to the first-order model.

To facilitate an efficient all-sky survey for the observation of radio sources, a scheduling program was written and integrated within the OTF-mapping R&D system. Figure 13 is the output produced by the scheduling program for DSS 13, where each yellow dot represents a radio source to be observed and data recorded utilizing a 1-D cross-scan, as illustrated in Fig. 7. The gathered data are then processed by the fourth-order pointing model software, which computes a set of 59 coefficients that constitute the new pointing model for the antenna (a future article in this publication will address the fourth-order pointing model in detail). For now, we want to present only the final proven results. When the derived model was applied to the DSS-26 BWG antenna at Goldstone and used in operational activity to track Voyager 1, a new performance level record of 3.5-mdeg MRE was achieved. This was previously never attained on any of the 34-m BWG antennas (a typical performance level of these antennas was 7 to 10 mdeg MRE at best). The result of this track is presented in Fig. 14.

Another special characteristic of the data distribution of Fig. 14 is that, in addition to the low MRE value, the data have a zero mean. This is particularly interesting because, in prior residual pointing-error data plots, a sharp transition was observed as spacecraft moved across the meridian. This result was helpful in diagnosing the cause of that hysterisis and attributing it to an elevation encoder coupler.[14]

---

[13] D. Rochblatt, P. Richter, and P. Withington, "Precision Blind Pointing Calibration of the NASA-JPL-DSN Large Reflector Antennas at Ka-Band (32-GHz)," NTR 41106 (internal document), Jet Propulsion Laboratory, Pasadena, California, April 2006.

[14] *1st DSN Antenna Calibration Workshop*, JPL D-29992 (internal document), Jet Propulsion Laboratory, Pasadena, California, July 6–9, 2004.
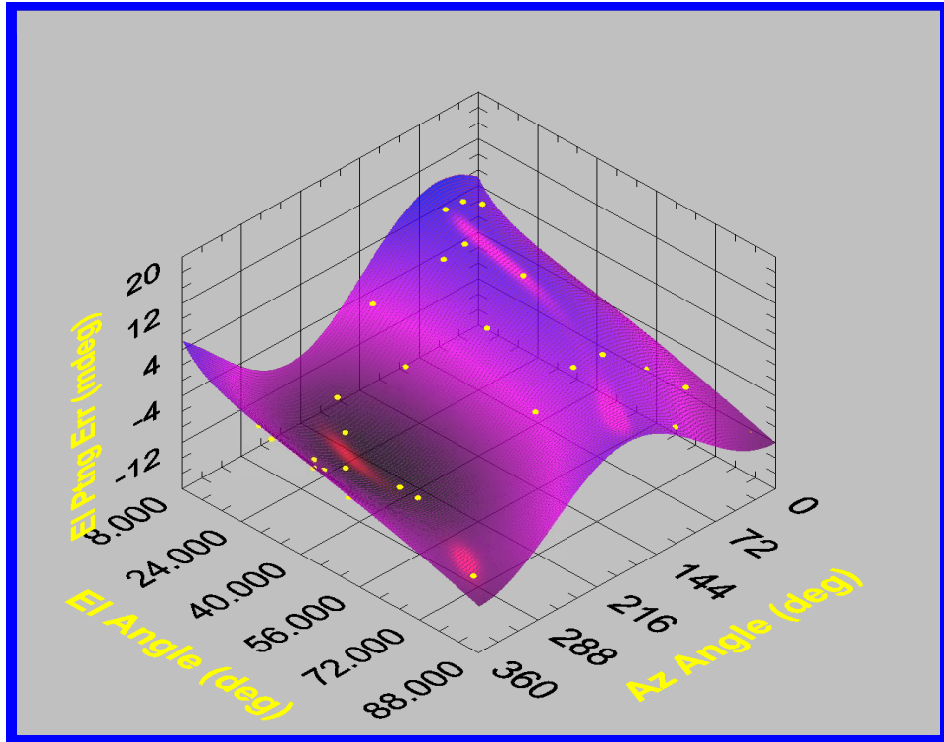
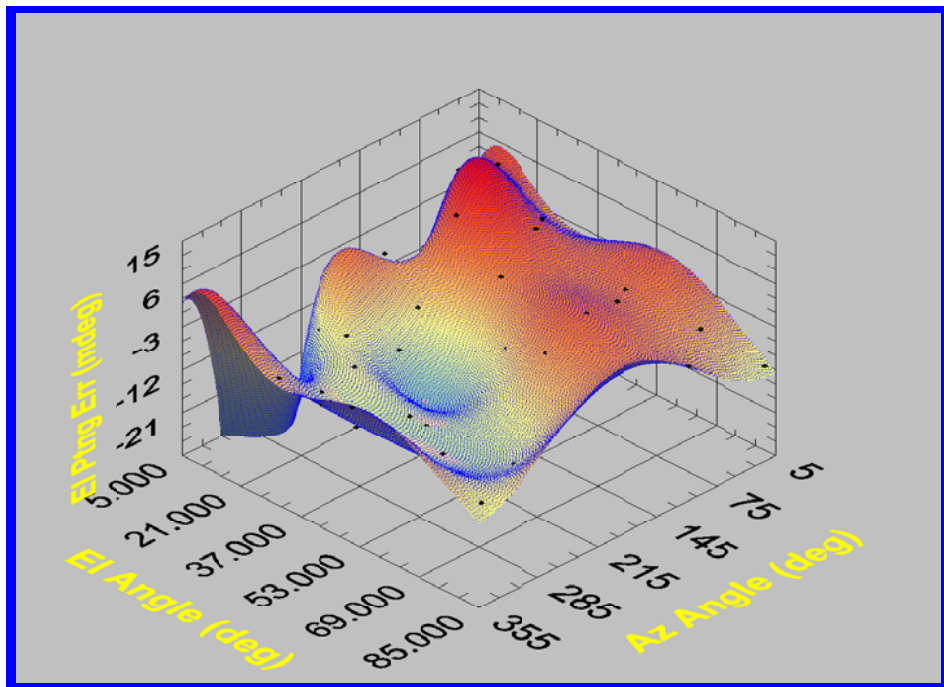**Fig. 11. Traditional first-order pointing model, resulting in 2.74-mdeg MRE.**

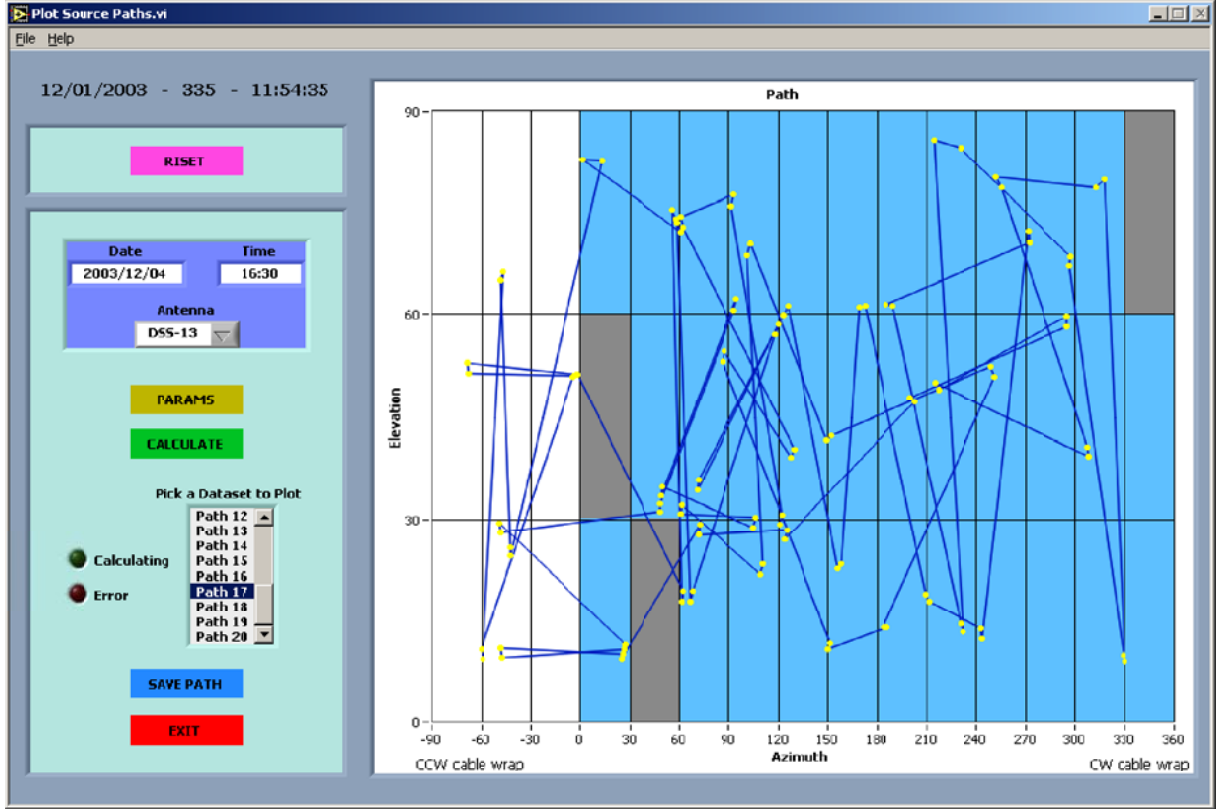**Fig. 12. New fourth-order pointing model, resulting in 1.49-mdeg MRE.**

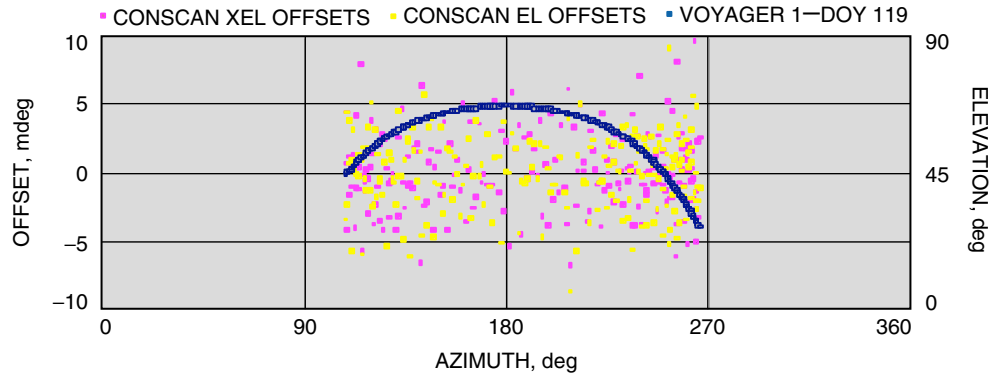**Fig. 13. OTF-mapping R&D scheduling display for efficient all-sky source selection and observation.**

Fig. 14. DSS 26 tracking Voyager 1 with 3.5-mdeg MRE using the fourth-order model [2003, day of year (DOY) 119; model "day4th.sem"].

C. Cassini-Jupiter Microwave Observing Campaign

1. Introduction. The objectives of the radar instrument onboard the Cassini-Huygens spacecraft are to map the surface of Titan and to measure properties of Saturn's rings and atmosphere. However, utilizing the Cassini radar as a radiometer can provide invaluable information regarding the atmosphere and surface compositions of Saturn and its moons as well as Jupiter. However, the fact that the Cassini-Huygens onboard radar was not calibrated as a radiometer prior to launch was a deterrent for making such high-accuracy measurements. The flyby of the Cassini-Huygens spacecraft past Jupiter in December 2000

provided an opportunity to calibrate the onboard radar as a radiometer, utilizing Jupiter as its known temperature load. The accuracy with which the Jupiter disk temperature could be determined from ground observations would translate directly to the accuracy of the calibration of the onboard radiometer and, consequently, would determine the accuracy with which atmosphere and surface measurements of Saturn and Titan could be made. The fact that the Cassini onboard radar operates at 13.78 GHz was an additional challenge since none of the JPL–DSN ground antennas was equipped with a feed at this exact frequency.

The strategy for the measurements and calibrations was laid out in 1999.[15] The goal was to measure Jupiter's disk temperature with a 1-sigma accuracy of 2 percent, which, if it could be achieved, would enable new science. The technique was based on performing high-accuracy ground-based calibration measurements simultaneously with the spacecraft observations and in the exact same frequency of 13.78 GHz. This allows us to transfer to the Cassini radar receiver the ground-based radio astronomy flux calibration with high accuracy, using Jupiter as a common reference source. What made this calibration challenging is the fact that absolute calibration measurements of radio sources near 13 GHz do not exist. Current estimates of the absolute uncertainty of the radio astronomy flux calibration scale tend to increase with frequency in the centimeter-to-millimeter radio astronomy bands. Typical estimates of systematic errors in radio source flux measurements near 5 GHz are ∼2 percent (1 sigma), whereas the estimates near 22 GHz are ∼10 percent (1 sigma).

To achieve the maximum accuracy, a ground-based TPR was designed, built, and installed at DSS 13 (Fig. 2), a 34-m BWG R&D antenna, while incorporating the OTF-mapping R&D system technique described above. After the installation of the TPR, and to support these in-flight calibrations, a coordinated series of ground-based observations named the Cassini-Jupiter Microwave Observing Campaign (Cassini-JMOC) was carried out from November 2000 through March 2001.

The second objective of the Cassini-JMOC Project included an educational component that allowed middle- and high-school students to participate directly in the ground-based observations and data analysis. The students made their observations as part of the Goldstone Apple Valley Radio Telescope (GAVRT) Project.

2. Observations. The 34-m GAVRT antenna was used to participate in a multi-frequency campaign to study Jupiter's synchrotron radiation [15]. GAVRT students and teachers teamed with professional scientists and engineers to measure the ratio of Jupiter's flux density relative to those of six calibration sources that were selected to mitigate different sources of random and systematic errors. The calibration-source selection criteria included the following:

(1) Flux density should be greater than 2 Jy to ensure high signal-to-noise ratio (SNR), $5 < \text{SNR} < 10$, for individual measurements.

(2) Spectral index should be *known* with sufficient accuracy to interpolate the flux density at 13.8 GHz.

(3) Angular size should be small compared to 0.039 deg (the 3-dB width of the 34-m antenna beam at 13.8 GHz).

The source 3c405 (Cygnus A) was *exempted* from these selection criteria because it is one of the sources that is also being measured directly from Cassini during special calibration sequences in the fall of 2000 and at other times during the mission. There is evidence that the source does not vary with time and that its circular polarization is small (4 percent). Its proximity to Jupiter's location on the sky (right ascension and declination) was an advantage. All measurements of Jupiter and the calibration sources

[15] D. Rochblatt, Presentation to M. Klein and M. Janssen (internal document), Jet Propulsion Laboratory, Pasadena, California, May 7, 1999.

were processed to remove sources of error caused by changes in system performance with antenna tracking in azimuth and elevation. System mini-calibration sequences were performed about three times per hour to monitor subtle changes in receiving system gain, stability, and linearity.

3. Results. Tests were conducted in April 2001 at DSS 13 using the OTF-mapping R&D instrumentation to observe Venus, Jupiter, 3c405, 3c273, 3c274, 3c286, NGC7027, 3c123, and 3c84. Given that the antenna half-power beamwidth (HPBW) for the 34-m antenna operating at 13.8 GHz is approximately 0.041 deg, the raster dimensions were scaled for approximately three times the HPBW to produce maps with spatial dimensions of 0.125×0.125 deg on the sky. The temporal resolution along the scan corresponded to about 1/10 HPBW (approximately 0.004 deg), which resulted in data arrays of 33×33 points (Fig. 8). Typical raster scans required 15 to 20 minutes to complete. When the weather was calm, excellent raster alignment was achieved. However, when the wind speed was above 17 km/h, apparent misalignment in the raster was observed (see the raster data at 34.3-deg elevation in Fig. 15). The source of this problem is believed to be subreflector ascillations because no apparent misalignment in the antenna angle encoder registering was noticed.

In deriving the DSS-13 antenna efficiency, the OTF-mapping R&D system was used while tracking 3c273 (point source) and 3c274 (calibrated source), both obtained near the rigging angle of 49 deg, where an efficiency of 61 ± 2 percent was computed. Then the OTF-mapping data of Venus, obtained from 8.7- to 58-deg (Fig. 15) elevation, also was calibrated at 49-deg elevation to that value. In the process, a source-size correction of 1.070 was computed for 3c274 near the same rigging angle, which compares well with the independently derived value of 1.075, obtained using the other scanning techniques that required many more observations.

The data and the plots demonstrate the capability of the OTF-mapping R&D system to reveal distortions in the antenna beam pattern at low elevation angles, as is clearly shown at 8.7- and 12.7-deg elevations. These distortions are due to gravity-induced deformation of the main reflector surface [16]. At 8.7 deg, the antenna pointing error caused the image to be off center. The mispointing of the antenna is due in large part to errors in estimating the refraction correction at such a low elevation angle.

Figure 16 illustrates the stages of data processing for the OTF-mapping R&D system. Figure 16(a) shows the 2-D response of the raster scan data taken across Venus when it was near 58-deg elevation. The plot was constructed after removing the background noise, which is fitted to a 1-D baseline with arbitrary slope [Eq. (21)]. Venus was close to Earth and, therefore, it was a very strong radio source when the measurements were made. Consequently, the noise level in the map is very low, and the smooth surface of the 2-D plot indicates the excellent alignment of the individual raster sub-scans. The x- and y-axis coordinates correspond to elevation (EL) and cross-elevation (XEL) of the maps. The samples along the subscan direction are approximately 0.0039 deg. The z-axis shows the measured system noise temperature in kelvins. Figure 16(b) is the result of fitting the raw data with an Airy function [Eq. (20)]. The mathematical expression that describes the spatial smoothing is caused by diffraction when radio waves (or light waves) are reflected off a circular aperture, which in this case is the 34-m effective-parabolic dish. The formal equation for diffraction of radio antennas is the Jacobi–Bessel series expansion of the far-field pattern of the antenna.
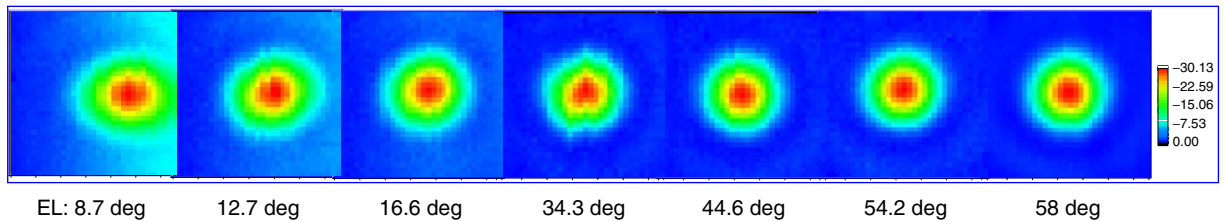

EL: 8.7 deg   12.7 deg   16.6 deg   34.3 deg   44.6 deg   54.2 deg   58 deg

Fig. 15. A series of patterns taken of Venus at source elevations from 58 to 8.7 deg, with T_a (K) versus XY.
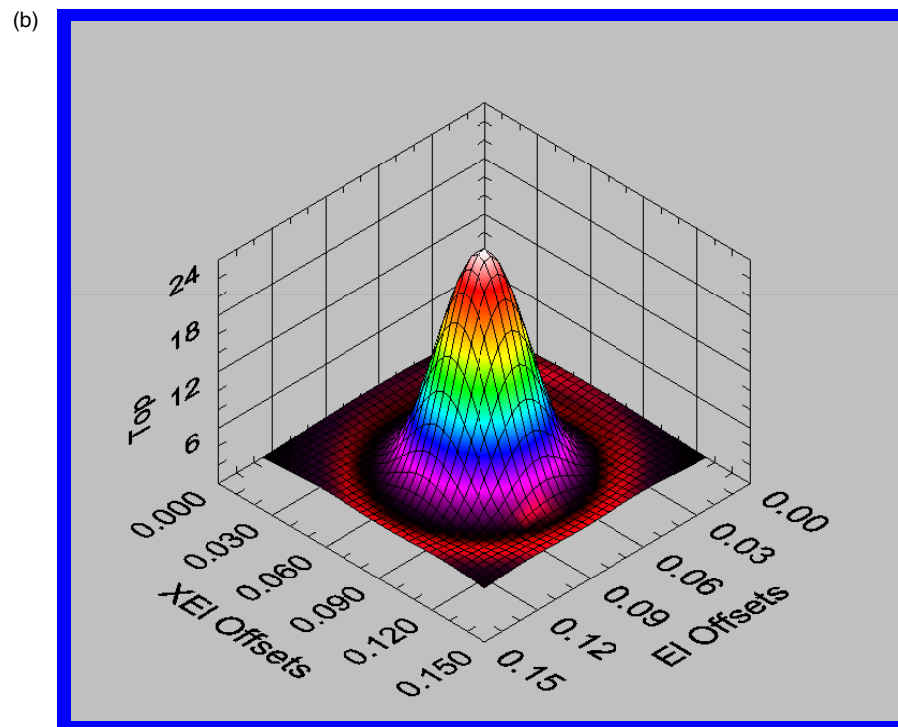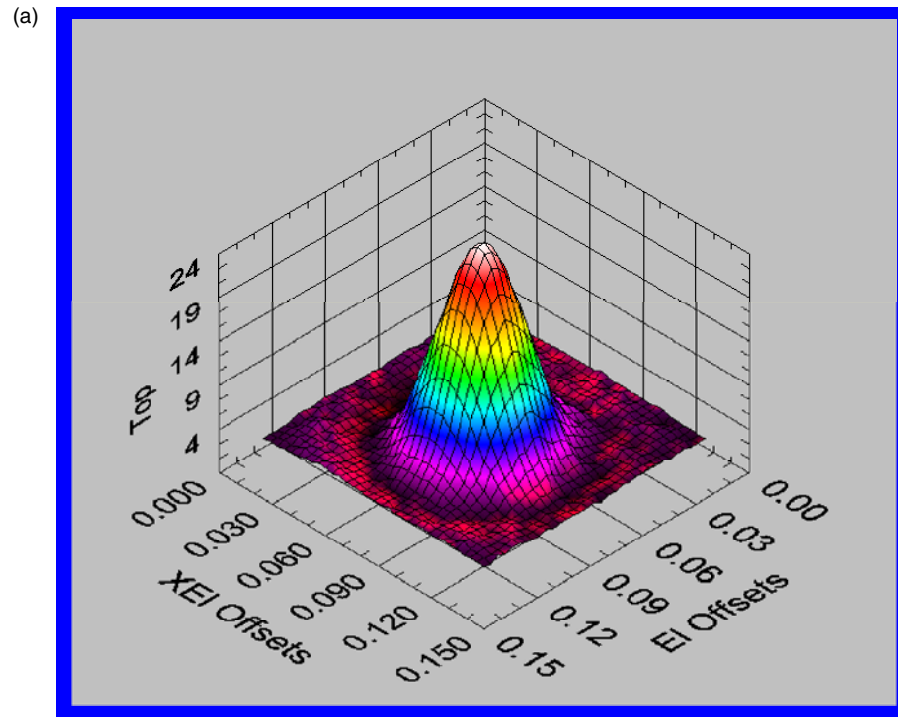
(a)

(b)

Fig. 16. The stages of data processing for the OTF-mapping R&D system: (a) the 2-D response of the raster scan data taken across Venus when near 58-deg elevation and (b) the result of fitting the raw data with an Airy function.

Figure 17 shows the data processing of OTF-mapping data of 3c405, Cygnus A, using DSS 13. Since 3c405 is an extended source for this antenna at 13.8 GHz, the convolution of the source with the antenna main beam resulted in the image on the top left and lower left of Fig. 17. The lower right corner of this figure displays the Airy pattern model of the antenna main beam. After the subtraction of the main beam from the data, the double-lobed shape of Cygnus A is revealed. A VLBI image of Cygnus A taken by the Very Large Array (VLA) is shown in Fig. 18 for reference. The criticality of a 2-D raster scan for accurate determination of source-size correction is clearly demonstrated by this process.

The observed ratios of Jupiter to the six calibration sources were used to calculate the effective disk temperature of Jupiter from each calibrator. The spectral indices of Venus and the sources 3c286, 3c123, and NGC 7027 were updated with new results from the National Radio Astronomy Observatory (NRAO). The result is shown in Fig. 19. The average disk temperature was computed to be $165 \, K \pm 2 \, K$, signifying an accuracy of 1.2 percent, which exceeds the project goal. This accuracy translates directly to the accuracy with which the Cassini radar can be used as a radiometer to study the atmosphere and surfaces of Saturn and its moons. Most notably, these results were possible due to the new set of observations being carried out at Goldstone to map the brightness distribution of 3c405 and 3c274 using the OTF-mapping technique described above. If these observations were to be made by conventional autobore measurement techniques, an accuracy of only 4.3 percent would have been achieved [17]. The raster scan technique reduces the uncertainty in the total flux density measurement that arises when the antenna beam partially resolves the spatial dimensions of an extended radio source.

VI. Operational Antenna Calibration and Measurement Equipment for the DSN

The OTF-mapping R&D system provided complete functionality in a portable package; however, it did not provide the best architecture for an operational DSN environment. It was desirable to have an antenna calibration system that could provide all these functionalities from the centralized DSN Signal Processing Center (SPC) and interface with the network monitor and control (NMC) of the DSN subsystem. The Antenna Calibration and Measurement Equipment (ACME) was designed to run over the SPC local area network (LAN) without modifying operational environments.

The other key design feature of the operational system that is different from its R&D predecessor is its synchronization implementation. It is based on position and timing in the R&D system (Section IV.B), but ACME synchronization is based on time alone. The time synchronization is provided by computing
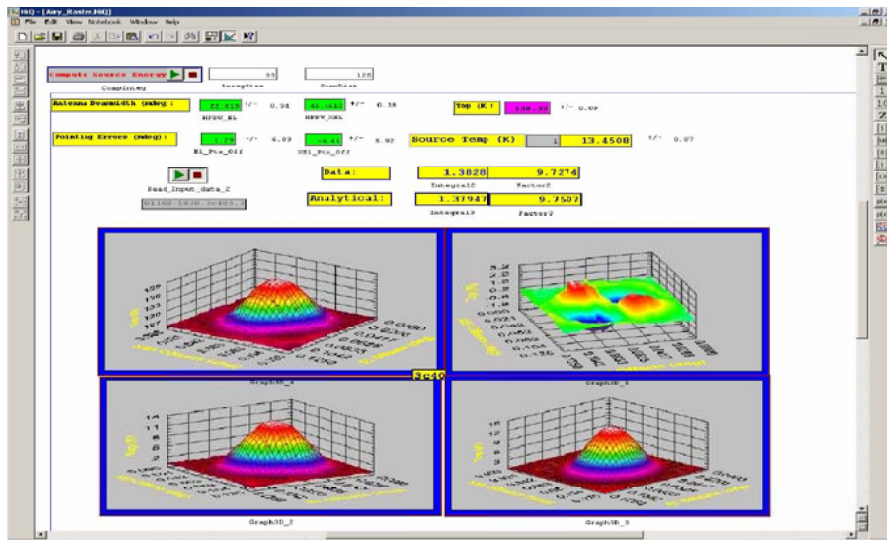

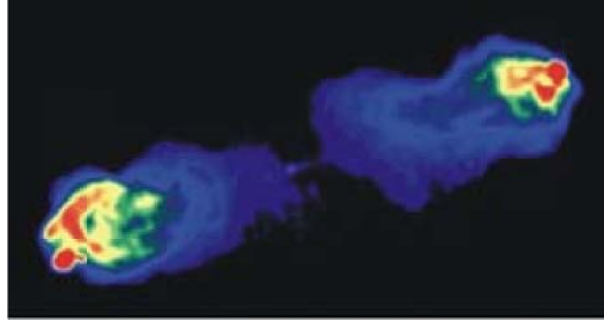**Fig. 17. 3c405, Cygnus A, mapping by a single 34-m antenna at 13.78 GHz.**

Fig. 18. Cygnus A. Image courtesy of NRAO/AUI/NSF, Investigator: Rick Perley.
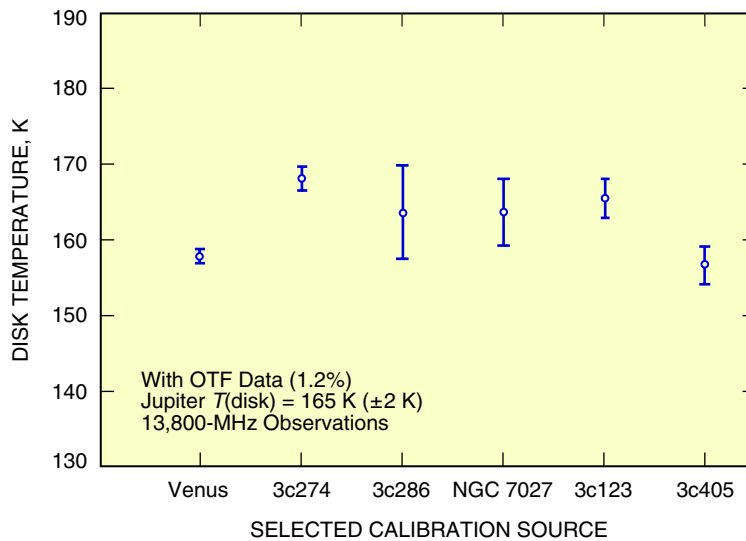

Fig. 19. Jupiter disk temperature determined by the OTF-mapping technique.

a predict file for the antenna controller that describes the exact antenna positions relative to the radio sources during a complete raster (for either the 1-D or 2-D scans) as a function of absolute time. These time stamps within the predict file provide the synchronization with the radiometer recorded values. A block diagram of the ACME interface in the DSN environment is shown in Fig. 20.

A. ACME Major Capabilities

ACME uses noise-adding radiometer (NAR) techniques to compute system noise temperature (SNT) values that can be used to compute pointing offsets, antenna efficiency, and subreflector optimization for different feeds.

The two channels provided with the system enable simultaneous measurement of two frequency bands or two polarizations in the same band. This feature is especially useful in determining antenna beam coincidence at different frequency bands, and it greatly improves the productivity of the time devoted to calibration. The new system can be used to evaluate non-modeled phenomena, such as coupler hysteresis (EL or AZ different readings at the same position coming from different directions) and weather effects on
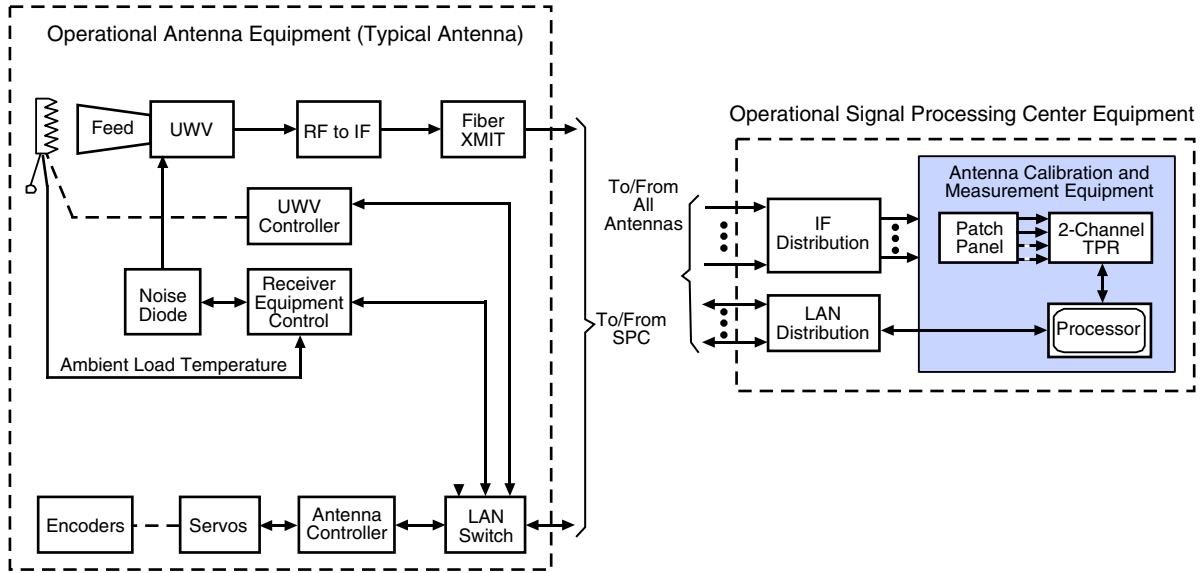
Fig. 20. ACME system block diagram.

antenna pointing performance. Surface deformations caused by temperature gradients, strong wind, and bad refraction correction are examples of possible weather interference in antenna pointing performance. In addition, the system can be used to measure the antenna track level unevenness and to detect servo anomalies. The system provides for the maintenance of pointing models from previous observations, for refining accuracy, and for general archiving of observation data for trend and historical data analysis.

B. Subsystem Design and Description

ACME is designed to perform the calibration activities by interfacing with the existing resources at the station and measuring the noise power with a square-law power meter. A single equipment rack is installed at each of the SPCs that interfaces with the antenna servos, microwave switches, noise diodes, and the antenna controller through predict distribution. Software uses current communication protocols used on the DSN SPC LAN.

The calibration activities are performed without changing the station operational configuration. This dramatically reduces the risk over the subsequent spacecraft tracking passes. The preparation time is small enough to allow use of virtually all antenna free times to obtain usable data. More calibration data will be available in the next years to increase the knowledge of the station calibration status, the degradation rates, and a number of hitherto unknown factors that impact the pointing accuracy and efficiency of the antenna.

The power measurements are being carried out by a set of band-limited filters of 5 percent bandwidth (BW) and using broad bandwidth square-law detectors. Signals from the complex intermediate frequency (IF) switch distribution allow for selection of any front end, and they can be applied to a filter bank with center frequencies of 250 MHz (BW = 12.5 MHz), 321 MHz (BW = 16 MHz), or a tunable filter from 200 to 400 Mhz (BW = 5 percent).

ACME uses NAR [18] techniques with the 50-K diode to calibrate operational parameters. The process is highly automated and does not require any manual intervention for configuration. The radio source catalog from year 2000 is maintained within the system, and it computes nutation, precession, and diurnal and annual aberration to determine current position and to build cosine director-type predicts for later antenna controller distribution and synchronization. When executing continuous scans, the width of

each scan typically is set up to five times the HPBW over the source. The system radiometer measures and integrates noise power to derive a far-field antenna pattern over a calibrated rectangular coordinate system, normally elevation versus cross-elevation.

C. Radiometer Calibration

Power measurements are derived by switching a 50-K diode as reference over ambient load and sky in a NAR [19,20] mode. Microwave switch configurations as well as diode-modulating control signals are fully automated under ACME control. The precision achieved during measurement of total power is 1 percent, and while operating in a NAR mode it is 1.2 percent (Fig. 21).

D. Pointing Measurements

As of today, pointing is the main application of ACME. As the DSN moves up its operating frequency, pointing precision becomes more and more relevant. The calibration system must maintain systematic error models and be able to collect data in a variety of conditions without interfering with the DSN operations schedule. ACME performs these functions, and it is able to give an overall picture of pointing quality in less than 5 hours under normal weather conditions.

ACME is operated with a user-friendly graphical user interface (GUI). Clicking over a source on the general source display map (Fig. 22) causes the given source to be added to a source list for a given session observation. The predicts are built for the sources on the list for later distribution to antenna controllers that will direct antenna movements to scan the sources.

The main computations engine of the system is based on a nonlinear Levenberg–Marquardt regression using Eqs. (20) and (21) (Fig. 23), from which SNT values are derived from measured data. The composition of the two-axis (EL and XEL) scan gives to the system the basic data for calibration: The center of the scan is the theoretical position of the radio source. From the distance of the maximum noise power relative to the center of the scan, the position error of the antenna in the measured axis is computed. The baseline of the noise is the background noise, so the curve T_{op} is the source temperature measured with the antenna. If the source is an accurately modeled radio source, the antenna efficiency can be derived from this measurement. The width of the curve at the -3 dB level is the main-beam HPBW.
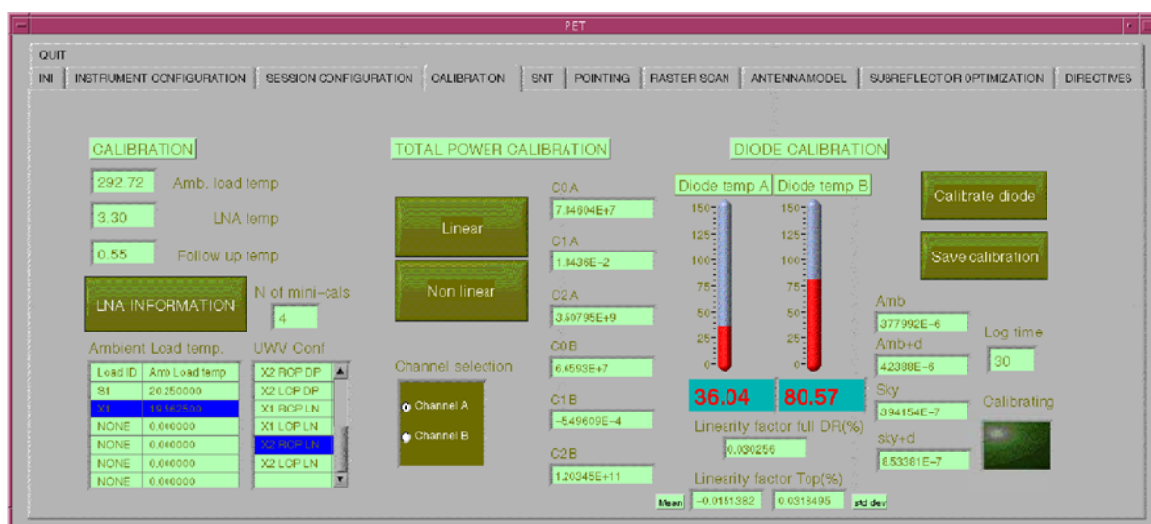

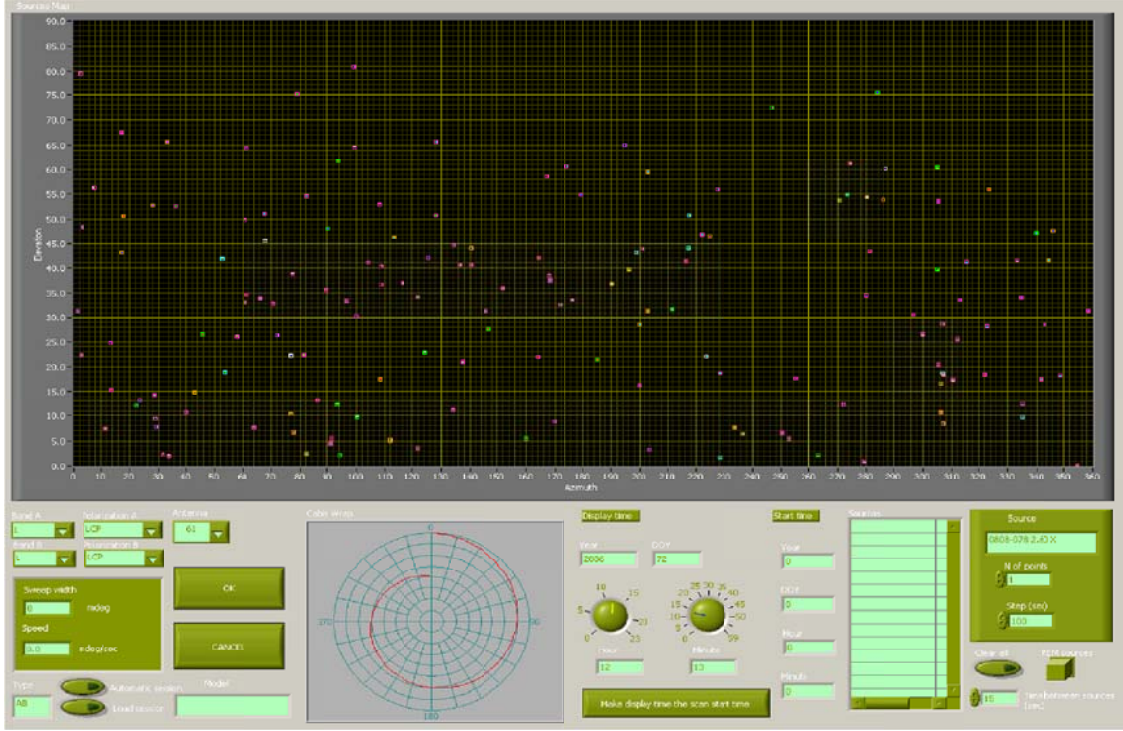**Fig. 21. ACME calibration GUI.**
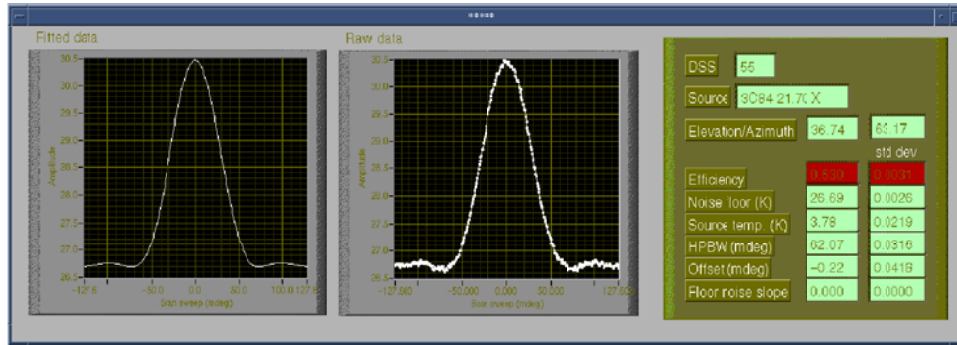
Fig. 22.   ACME GUI for radio source selection.

Fig. 23.   1-D scans, with raw data shown on the right side and
the fitting function on the left side.

Data derived from computed offsets are used to derive either a first- or fourth-order systematic error model. ACME provides a model calculator that can read data from the system or other sources. In addition, it provides an input filter to apply to input data. Another feature is the ability to "fill" empty areas of the sky with data from previously built models.

E. Subreflector Optimization

Subreflector misalignment translates into antenna efficiency loss. The Ruze equation gives an expression for this loss:

$$\eta = e^{-(4\pi\varepsilon/\lambda)^2} \tag{31}$$

where ε is proportional to the subreflector displacement [21].

To determine the optimal subreflector position, ACME determines the maxima of the curves derived from the subreflector movement over the selected axis. Two orthogonal scans are performed for every position (Fig. 24).

The equation used to calculate loss of efficiency derived for small pointing errors is

$$T = T_0 \cdot e^{-(2.273 \cdot \theta^2 / \text{HPBW}^2)} \tag{32}$$

F. Future Work

ACME in its first delivery has three main goals:

(1) Radiometer calibration, SNT measurements

(2) Pointing tool (pointing measurement and systematic error-model derivation)

(3) Subreflector focusing

Important improvements for the next deliveries will increase the productivity of the tool and enable accurate measurement of the antenna efficiency. In the current version of the software, the pointing sessions have to be scheduled manually. Depending on the experience and ability of the system operator, the number of sources scheduled in a certain period of time will be different. Therefore, the scheduling routine of the OTF-mapping R&D system will be integrated into ACME. The routine will focus on the stronger sources and, when they not available, will integrate longer on the weak sources.

The raster scan is the basic tool to determine efficiency with accuracy. Based on the fitting of the far field of the antenna to the 3-D Airy function, the real flux of the source can be derived. Accurate raster scans will be implemented, as well as a routine to derive the source-size correction factor and the antenna efficiency.

The database will be increased, and the calibration historic data will be presented in a friendly mode to get a quick picture of the history of the antenna. A Web server will be implemented in every station, and the connectivity with a central database will be automated whenever new data are collected.
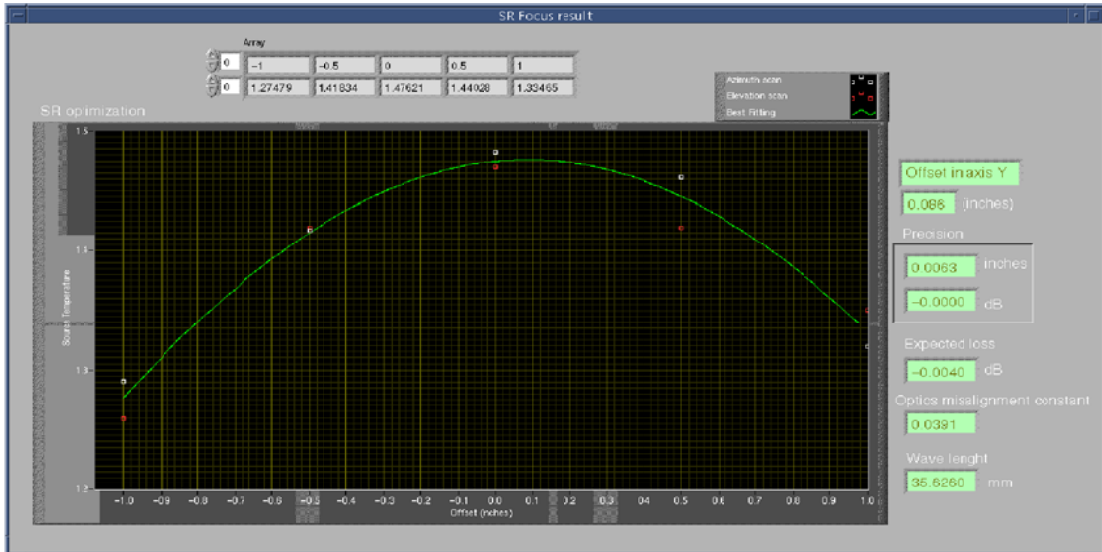

Fig. 24. ACME subreflector optimization GUI display.

As the system begins to be used by the final users at the stations, more feedback is expected, and more and better improvements will be added to the future work.

VII. Conclusions

A theoretical analysis of gain and pointing calibration methods, together with a realistic assessment of system noise characteristics, has led to the conclusion that significant improvement in performance can be realized by performing rapid, continuous raster scans of point and extended radio sources, and determining temperature and pointing information from two-dimensional, nonlinear, least-squares fits of the data to realistic beam patterns.

The method has the further advantage that source-size corrections, which presently represent a significant source of error in both gain measurements and source flux density determinations, are not needed since essentially all of the source flux density is collected during the raster scan.

The use of rapid scanning also results in the collection of vastly more data than with conventional techniques, so that errors in gain or in aperture efficiency versus elevation curves can be greatly reduced.

Measurements at Ku-band and Ka-band, based on 1-D and 2-D fitting, are in good agreement with theoretical calculations using measured power spectral density data to predict the background noise during a scan, and using this background noise as input to a nonlinear, least-squares model to predict fitting parameter errors.

This application of the OTF-mapping R&D system for the Cassini-JMOC calibration work demonstrates some of the valuable attributes of the system for the calibration and performance analysis of the DSN antennas for telemetry and for radio science.

The OTF-mapping R&D system has been developed into an operational antenna calibration system (ACME). ACME initial delivery is the first step in an ambitious project to provide the DSN with a standard calibration tool. This is the first attempt to use a unified evaluation criterion, allowing larger quantities of data to be collected and improving their quality. It will allow the technical community to know the state and evolution of all antennas by means of a common database. Setup of the tool is quick and operationally safe. Calibration times depend on the type of measurements, but experience gathered so far indicates that it will easily be made compatible with DSN routine maintenance and operations.

As the system is used by the stations' calibration engineers, more feedback is expected, and more and better improvements will be added to the future work.

ACME relies heavily on current subsystems and interfaces. Antenna position is determined by means of predicts, without an actual reading of the antenna encoders. Similarly, microwave switch configurations fall on the respective controllers. Noise diode status and control fall on the downlink channel. Maintenance of these interfaces will be necessary to maintain the fully operative system.

Acknowledgments

References

[1] J. Bautista, R. Clauss, S. Petty, and J. Shell, "DSN Low Noise Amplifiers in the New Millennium, *IND Technology and Science Program News*, Jet Propulsion Laboratory, Pasadena, California, Issue 13, Rev. 1, January 2001.

[2] M. P. Godwin, A. J. T. Whitaker, and A. P. Anderson, "Microwave Diagnostics of the Chilbolton 25-m Antenna Using OTS Satellite," *Proc. Inst. Elec. Eng. Int. Conf.*, York, England, pp. 232–236, 1981.

[3] D. J. Rochblatt and B. L. Seidel, "DSN Microwave Antenna Holography," *The Telecommunications and Data Acquisition Progress Report 42-76, October–December 1983*, Jet Propulsion Laboratory, Pasadena, California, pp. 27–42, February 15, 1984. http://ipnpr/progress_report/42-76/76C.PDF

[4] D. J. Rochblatt and B. L. Seidel, "Microwave Antenna Holography," *IEEE Trans. Microwave Theory and Techniques*, Special Issue on Microwaves in Space, vol. 40, no. 6, pp. 1294–1300, June 1992.

[5] D. J. Rochblatt and Y. Rahmat-Samii, "Effects of Measurement Errors on Microwave Antenna Holography," *IEEE Trans. Antennas Propagation*, vol. 39, no. 7, pp. 933–942, July 1991.

[6] J. W. M. Baars, R. Genzel, I. I. K. Pauliny-Toth, and A. Witzel, "The Absolute Spectrum of Cas A; An Accurate Flux Density Scale and a Set of Secondary Calibrators," *Astron. Astrophys.*, vol. 61, pp. 99–106, 1977.

[7] M. J. Klein and C. T. Stelzried, "Calibration Radio Sources for Radio Astronomy: Precision Flux Density Measurements at 2295 MHz," *Astron. Journal*, vol. 81, no. 12, pp. 1078–1083, 1976.

[8] P. H. Richter and S. D. Slobin, "DSN 70-Meter Antenna X- and S-Band Calibration Part I: Gain Measurements," *The Telecommunications and Data Acquisition Progress Report 42-97, January–March 1989*, Jet Propulsion Laboratory, Pasadena, California, pp. 314-351, May 15, 1989.
http://ipnpr/progress_report/42-97/97GG.PDF

[9] J. D. Kraus, *Radio Astronomy*, New York: McGraw-Hill, pp. 97–101, 1966.

[10] B. L. Ulich and R. W. Haas, "Absolute Calibration of Millimeter-Wavelength Spectral Lines," *ApJS*, vol. 30, 1976.

[11] P. H. Richter, "Estimating Errors in Least-Squares Fitting," *The Telecommunications and Data Acquisition Progress Report 42-122, April–June 1995*, Jet Propulsion Laboratory, Pasadena, California, pp. 107–137, August 15, 1995. http://ipnpr/progress_report/42-122/122E.pdf

[12] R. N. Treuhaft and G. E. Lanyi, "The Effect of the Dynamic Wet Troposphere on Radio Interferometric Measurements," *Radio Science*, vol. 22, no. 2, pp. 251–265, 1987.

[13] D. Rochblatt, P. Richter, and P. Withington, "On-the-Fly Mapping for Calibrating Directional Antennas," *NASA Tech Briefs*, NPO-30648, vol. 28, no. 8, pp. 53–55, August 2004.

[14] D. Rochblatt and P. Withington, "Precision Blind Pointing Calibration of the NASA-JPL-DSN Large Reflector Antennas at Ka-Band (32-GHz)," EuCAP 2006—European Conference on Antennas and Propagation, Session 4A10A—Antenna Measurements (12j), November 9, 2006.

[15] S. J. Bolton, M. Janssen, R. Thorne, S. Levin, M. Klein, S. Gulkis, T. Bastian, R. Sault, C. Elachi, M. Hofstadter, A. Bunker, G. Dulik, E. Gudim, G. Hamilton, W. T. K. Johnson, Y. Leblanc, 0. Liepack, R. McLeod, J. Roller, L. Roth, and R. West, "Ultra-Relativistic Electrons in Jupiter's Radiation Belts," *Nature*, vol. 415, pp. 987–991, February 28, 2002.

[16] D. J. Rochblatt and B. L. Seidel, "Performance Improvement of DSS-13 34-Meter Beam-Waveguide Antenna Using the JPL Microwave Holography Methodology," *The Telecommunications and Data Acquisition Progress Report 42-108, October–December 1991*, Jet Propulsion Laboratory, Pasadena, California, pp. 253–270, February 15, 1992. http://ipnpr/progress_report/42-108/108S.PDF

[17] M. J. Klein, S. J. Bolton, A. J. Freiley, S. Gulkis, M. A. Janssen, S. J. Levin, D. J. Rochblatt, J. P. Roller, and R. K. McLeod, "DSN and GAVRT Observations of Jupiter at 13 GHz and the Calibration of the Cassini Radar Instrument for Passive Radiometry," URSI General Assembly, Naastrichthe, Netherlands, August 17–24, 2002.

[18] C. Stelzried, "Noise Adding Radiometer Performance Analysis," *The Telecommunications and Data Acquisition Progress Report 42-59, July–August 1980*, Jet Propulsion Laboratory, Pasadena, California, pp. 98–106, October 15, 1980. http://ipnpr/progress_report/42-59/59N.PDF

[19] C. T. Stelzried, "Correction of High-Frequency Noise-Temperature Inaccuracies," *The Telecommunications and Data Acquisition Progress Report 42-111, July–September 1992*, Jet Propulsion Laboratory, Pasadena, California, pp. 269–277, November 15, 1992. http://ipnpr/progress_report/42-111/111W.PDF

[20] C. T. Stelzried, "Noise Temperature and Noise Figure Concepts: DC to Light," *The Telecommunications and Data Acquisition Progress Report 42-67, November–December 1981*, Jet Propulsion Laboratory, Pasadena, California, pp. 100–111, February 15, 1982. http://ipnpr/progress_report/42-67/67N.PDF

[21] R. Levy, *Structural Engineering of Microwave Antennas*, Piscataway, New Jersey: IEEE Press, 1996.

[22] P. Stumpff, translation of "Astronomische Pointing Theorid fuer Radioteleskope," *Klein Heubacher Berichte*, vol. 15, Fornmolde Technischon Zentralamt, Darmstadt, pp. 432–437, 1972.